Ultra-fast light-induced (magnetic) skyrmion nucleation in ultrathin films

Auteur : Mignolet, Maxime
Promoteur(s) : Dupé, Bertrand; Verstraete, Matthieu
Faculté : Faculté des Sciences appliquées
Diplôme : Master en ingénieur civil physicien, à finalité approfondie
Année académique : 2021-2022
URI/URL : http://hdl.handle.net/2268.2/16289

University of Liège - Faculty of Applied Sciences

Ultra-fast light-induced (magnetic) skyrmion nucleation in ultrathin films

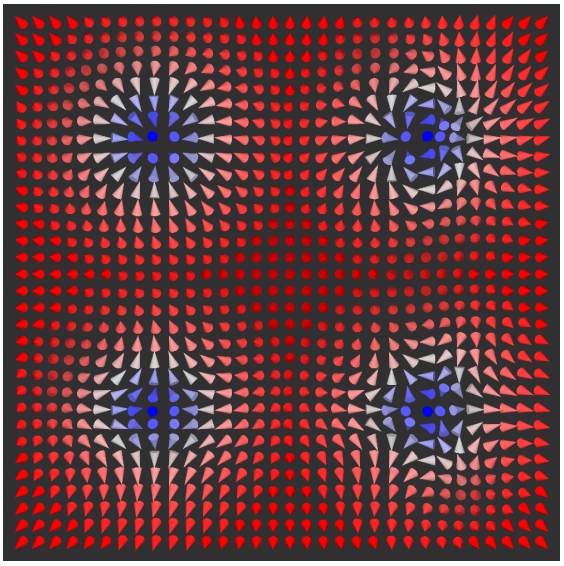

Master's thesis completed in order to obtain the degree of
Master of Science in Physics Engineering,
by Maxime Mignolet.

Supervisors: Bertrand Dupé
Matthieu Verstraete
Advisor: Louise Desplat

Academic year 2021-2022

Abstract

Magnetic skyrmions are topologically non-trivial particle-like magnetic textures. Possible applications encompass ultradense magnetic memories and low power computing. Skyrmions are therefore of great interest. In this work, we focus on the nucleation of individual skyrmions in a controllable manner as this still represents a challenge to be tackled to enable the realization of the possible applications.

We explore two nucleation routes. The first is an electric field driven nucleation. The application of a pulsed out-of-plane electric field induces a modification of the Dzyaloshinskii-Moriya interaction which permits the nucleation of a single skyrmion on the 100-fs timescale.

The second route to nucleation considered is the use of Laguerre-Gauss light beams, which carry orbital angular momentum (OAM). The nucleation occurs through the interaction with the electromagnetic field of the beam. We succeed to nucleate a single skyrmion as well as a skyrmionium, target skyrmion and two skyrmions. We show that the OAM helps reduce the nucleation threshold.

During this work, we also developed and implemented a generic algorithm for the automatic identification of skyrmionic textures in order to treat simulation results.

Résumé

Les skyrmions sont des textures magnétiques topologiquement non triviales et localisées dans l'espace. Les skyrmions sont de grand intérêt de par leur possibles applications, tels que des mémoires magnétiques ultra-dense et le calcul à basse puissance. Dans ce travail, nous nous concentrons sur la nucléation contrôlée de skyrmions individuels étant donné que cela représente encore un défi à résoudre pour permettre la réalisation des possibles applications.

Nous explorons deux voies pour la nucléation. La première voie est la nucléation via un champ électrique. L'application d'un champ électrique hors-plan pulsé induit une modification de l'interaction de Dzyaloshinskii-Moriya. Cette modification permet la nucléation d'un skyrmion isolé à l'échelle de 100 fs.

Le deuxième procédé de nucléation considéré est l'utilisation de faisceaux de Laguerre-Gauss, ceux-ci possédant du moment angulaire orbital. La nucléation a lieu via l'interaction avec le champ électromagnétique du faisceau. Nous arrivons à nucléer un skyrmion isolé ainsi que un skyrmionium, target skyrmion et deux skyrmions ensembles. Nous montrons que le moment angulaire orbital aide à réduire le seuil de nucléation.

Pendant ce travail, nous avons également développé et implémenté un algorithme pour identification automatique de textures skyrmionic dans le but de traiter automatiquement les résultats de simulations obtenus.

Acknowledgement

First of all, I would like to thank Bertrand Dupé, Matthieu Verstraete and Louise Desplat for their support and advice throughout this thesis. I am grateful for the opportunity that you gave me to work on this subject. I am also very thankful for the general patience you shown me.

Coming next, I'd like to thank the whole Nanomat group for the cheerful atmosphere, and especially Sebastian Meyer for making sure that I stay well caffeinated.

Un grand merci va à ma famille et à mes amis qui m'ont sontenu pendant cette longue année, mais également tout au long de mes études. I thank Lou for making sure my stomach stays full and refilling it when empty. I also thank Alessia for their great mathematical advice and helping me debug my code.

Contents

List of Figures

Nomenclature

$2D$	Two dimensional
$2DEG$	2D electron gas
ASD	Atomistic spin dynamics
DMI	Dzyaloshinskii-Moriya interaction
$Fig.$	Figure
FM	Ferromagnetic
LG	Laguerre-Gauss (beam)
LLG	Landau Lifshitz Gilbert equation
MAE	magnetic anisotropy energy
OAM	Orbital angular momentum
$RKKY$	Ruderman–Kittel–Kasuya–Yosida
SOC	Spin orbit coupling
SP	Spin polarized
STM	Scanning tunneling electron microscopy

1 Introduction

1.1 State of the art

Spintronics is a field of research which aims to not only use the electrical charge of the electron but also its quantum spin. Its macroscopic manifestation was observed in 1988 [4] when the resistance of a Fe/Cr multilayer was changed as a function of the external magnetic field. This effect is called the Giant Magnetoresistance (GMR) and opened up the way to the manipulation of the resistivity via the magnetization. Since then, new effects have been discovered such as the spin torque which allows the manipulation of magnetic moments by polarized currents [56]. This concept has led to possible new devices such as the race track memory device, which allows 3-Dimensional data and fixed read/write heads [46]. The information is then encoded into magnetic domain walls. To avoid possible pinning of domain walls, the concept of racetrack was extended to skyrmions. As opposed to domain walls which are 1 dimensional magnetic textures, skyrmions are localized (0D) non-collinear magnetic textures which behave like particles [17].

Skyrmions are topologically non-trivial magnetic textures which are of great interest as information carriers in information technology. Potential applications include magnetic memories [54, 44], logic gates [63, 36] and even neuromorphic computing [58]. As compared to domain walls, skyrmions can be manipulated at lower current intensities, which would decrease power consumption [8, 62]. Furthermore, their small size (a few nm) allows for ultradense memories and logic devices [54].

These potential applications require the ability to control individual skyrmions. In particular one should be capable of nucleating, annihilating, detecting and manipulating skyrmions in order to write, delete, read and process information. Regarding the nucleation, Romming *et al.* [48] managed to nucleate single skyrmions in an ultrathin film in a reliable and controllable manner. The nucleation is

achieved through the local injection of spin-polarized (SP) currents using a scanning tunneling electron microscopy (STM) in conjunction with an external static magnetic field. They observed that both the SP current and the bias voltage influence the nucleation speed. In 2016, Hsu *et al.* [24] demonstrated that a non spin-polarized STM tip could generate an electric field and also nucleate a single skyrmion.

Even though these two experiments demonstrated the feasibility of controlled skyrmion nucleation through either a SP-current or an electric field, they have the drawback of requiring the use of an STM. Furthermore both experiments were carried out at low temperature (< 10 K). In 2017, Schott *et al.* [55] overcame these drawbacks by nucleating skyrmions at room temperature using electric field gating. Even though this represents a major step forward, it does not allow for the nucleation of individual skyrmions as the electric field is applied on a large area.

Instead of gating, the nucleation of skyrmions could be achieved using a laser. In this case, two distinct mechanism have to be considered: The Joule heating and the electric field created by the laser pulse itself. When the nucleation is caused by the joule heating due to the laser pulse, the process is stochastic and the nucleation is non-coherent [6, 7, 9]. This process can occur from a non-collinear state similar to a domain wall called a spin spiral in B20 compounds [6] and out of a collinear FM state [7, 9]. The latter is a more surprising effect as it involves the dynamical stabilization of skyrmions at finite temperature such as in MnSi [43] or the presence of chiral magnons [35].

Theoretically, the efforts to describe temperature-induced magnetization dynamics are numerous. They all converge to the so-called three temperature model [29], or other closely-related models [28], which considers three distinct temperature baths at different time scales. The first temperature bath is composed of the electrons. It reacts at the femto- or atto-second timescale to the laser pulse. It corresponds to thermally excited electrons which acts on the magnetization and the lattice vibrations. The second bath is the magnetization lattice which hosts thermal magnons on the 100 of fs timescale. Finally at the ps timescale, the phonon bath dissipates the thermal energy into lattice excitations.

Magnetization dynamics can be induced coherently by a laser's electromagnetic field [57]. In that case, the dynamics occur on the atto-second or the femto-second time scale which allows a drastic speed up of the writing process and possibly a better control of the magnetic textures via the angular momentum of light. Theoretically, direct control of magnetization via electric field has only recently been proposed in [12], where it has been shown that skyrmion nucleation can be induced by an electric field pulse of a few hundreds of femtoseconds.

Up to now in these efforts to seed skyrmions, only light with no angular momentum has been used. In this thesis, we explore the possibility of coherently

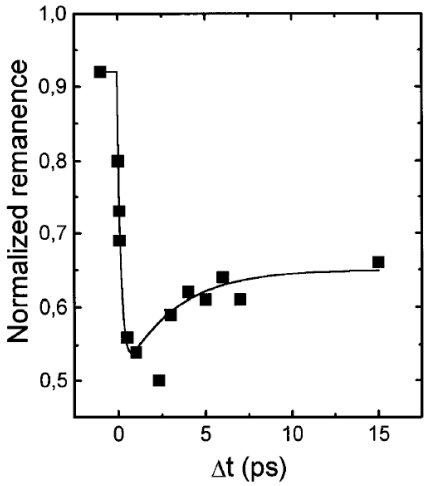

Figure 1.1: Demagnetization of a Nickel film from Ref. [5]

nucleating skyrmions using light carrying angular momentum. The nucleation occurs both via the electric and magnetic field of the light. The use of angular momentum is well suited for the nucleation of chiral structures, such as skyrmions, during which a transfer of angular momentum could occur.

1.1.1 Ultrafast Magnetization

In 1996, Beaurepaire and Bigot showed the loss of magnetization in Ni thin films due to a femtosecond laser pulse [5]. The observed loss of magnetization occurs at a surprisingly fast timescale of 50 to 300 fs. Fig. 1.1 shows this rapid decrease in magnetization after the application of the laser pulse. To explain this, Beaurepaire and co-workers divided the electrons, the spins and the lattice vibrations in three interacting subsystems (see the three temperature model in the next section). The electrons and the spins interact with each other at a timescale of about 50 fs [61, 45]. The spins and the lattice interact with a time constant of ~ 200 fs. It has recently been uncovered that polarized phonons play an essential role in this interaction as they act as a sink for energy and angular momentum [59].

To model such a process, it is convenient to use atomistic methods where the atomistic nature of matter is taken into account, as opposed to continuum methods where matter is considered as being a continuum. In that case, thermal excitations are taken into account via three stochastic processes, one for each of the subsystems (electrons, spins and lattice vibrations).

1.1.2 Modeling light matter interaction

The light-matter interaction can be studied in at least three different ways depending on the degree of detail and the involved energy- and time-scales. On the femto-second timescale electronic transitions occur, which can be described with fully quantum methods. Atomistic spin dynamics (ASD) is used for the coherent interaction with THz light at the 100-fs timescale, integrating away the electronic degrees of freedom. When used in conjunction with explicit thermostats or electric field coupling, ASD can also include temperature effects due to heating by larger frequency light, for which electronic transitions cause a significant heating. At larger time scales, the dynamics can be taken into account in an effective way by the three temperature model as a series of coupled heating processes.

Electronic transitions

In semiconductors as the photon energy approaches the energy of the band gap electronic interband transitions are more likely to occur. In metals, there is no reason that such transitions cannot occur at lower energy. When a photon is absorbed it will induce the transition of an electron from the ground state to a higher electronic band (see Fig. 1.2) [37]. This will bring the electrons out of equilibrium into excited states which can influence magnetization. As the electrons absorb the photons' energy, it will also bring heat to the system. It was found that such electronic transitions could be induced by phonon displacements and could even lead to a control of the magnetization in $La_{0.5}Sr_1.5MnO_4$ [18] and more recently in $DyFeO_3$ [1].

Atomistic spin dynamics

In atomistic spin dynamics localized atomistic spins are used to model the magnetization [15]. Although spins have quantum origins (e.g. quantized energy levels), we use a classical approximation, the Heisenberg model. Magnetic moments can take any orientation instead of discrete ones. We model their interaction using a Heisenberg Hamiltonian. The interaction with light occurs through its electric and magnetic field. The electric field induces a spin orbit coupling which acts indirectly on the spins [12]. Whereas the magnetic field interacts directly via Zeeman effect. These interaction are treated as non-thermal and are therefore coherent.

In this thesis, we will use atomistic spin dynamics as we aim to model coherent, non thermal magnetization dynamics induced by THz light. The ASD framework will be described in more details in chapter 2.

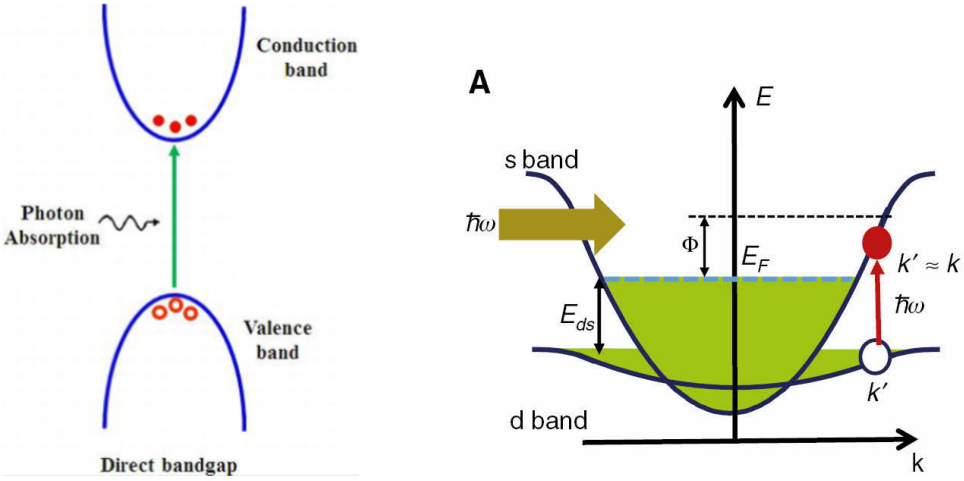

(a) (b)

Figure 1.2: Electronic transition in a semiconductor between valence and conduction bands (left), in a metal between d and s bands (right) in idealized solids. Figures taken from Refs. [20] and [31] respectively.

Three temperature model

In 1996 Beaurepaire *et al.* developed a three temperature model to explain the ultrafast loss of magnetization in Nickel due to a laser pulse [5]. In this model the electrons, the spins and the lattice form three interacting reservoirs, each with its own temperature and specific heat (see Fig. 1.3 (a)). The time evolution of the bath temperatures is described by the coupled equations:

$$\begin{aligned} C_e(T_e)dT_e/dt &= -G_{el}(T_e - T_l) - G_{es}(T_e - T_s) + P(t), \\ C_s(T_s)dT_s/dt &= -G_{es}(T_s - T_e) - G_{sl}(T_s - T_l), \\ C_l(T_l)dT_l/dt &= -G_{el}(T_l - T_e) - G_{sl}(T_l - T_s). \end{aligned} \tag{1.1}$$

where C_e, C_s, C_l are the specific heat of the electrons, spins and lattice and G_{es}, G_{el}, G_{sl} are the interaction constants. The light-matter interaction happens through the heating of the electrons. This is described via the term $P(t)$ in the electronic equation.

Fig. 1.3 (b) represents the time evolution of the temperature of the different sub-systems after the laser is applied. The electron temperature increases extremely fast, at the femtosecond time scale and can reach temperatures larger than 1000 K [27]. Heat is then transferred to the spin sub-system which results in the excitation of magnons at the 100-fs timescale and to the lattice at a much slower rate. The rise in temperature of the spins explains the loss of magnetization at the sub-picosecond timescale.

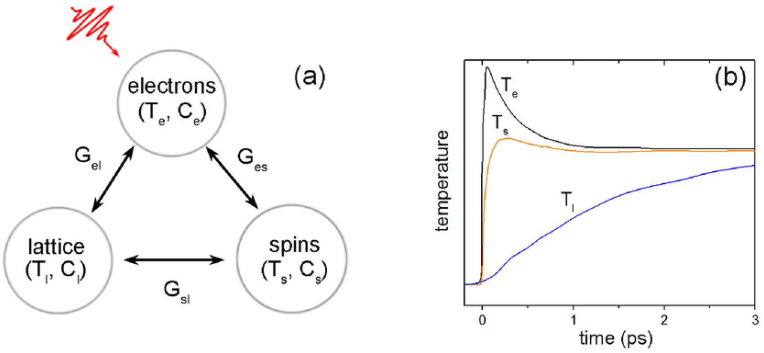

Figure 1.3: Three temperature model Reproduced from Ref. [27]

Essentially, the laser pulse brings the system out of equilibrium and should be treated correspondingly. However intra-system dynamics are presumed to act faster than inter-system dynamics such that each system quickly thermalizes and can be considered in equilibrium. This assumption is consistent with experimental data [5].

1.2 Magnetic ordering

1.2.1 Collinear magnetization

There are different collinear spin orderings. The simplest one is the ferromagnetic state. In this configuration all the atomic spins have the same magnetic moment and they are all pointing in the same direction (see Fig. 1.4 (a)). Another collinear ordering is the case of antiferromagnetism: one half of the spins are pointing in one direction and the other half in the opposite direction (Fig. 1.4 (b)). In this configuration the net magnetic moment of the material is zero. One last general example of collinear ordering is the ferrimagnetic state (Fig. 1.4 (c)). In this case we have two types of spins with different magnetic moments. One type is oriented in one direction and the other type in the opposite direction. As the two types of spin have different magnetic moment the net magnetization of the material is non-zero.

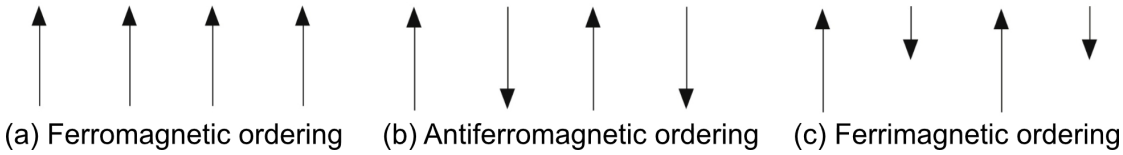

Figure 1.4: Collinear magnetic orderings. Adapted from Ref. [40]

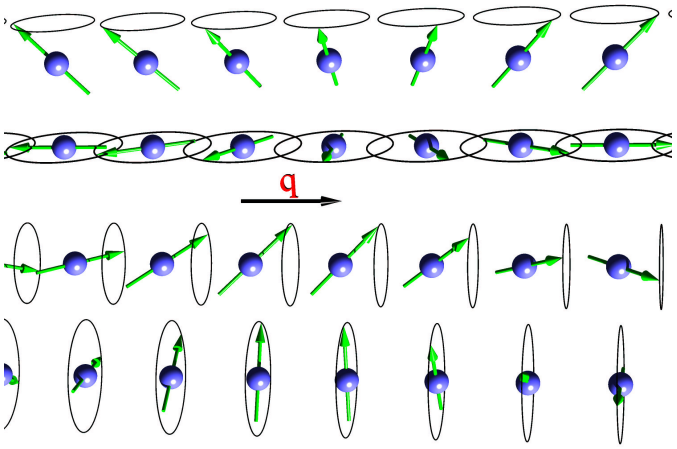

Figure 1.5: Different types of spin spirals. From top to bottom: conical spin spiral, flat conical or Néel spin spiral, cycloidal spin spiral, flat cycloidal or Bloch spin spiral. Image taken from Ref. [33].

1.2.2 Non-collinear magnetization

Other configurations, in which the spins are not all aligned with a single quantization axis, are termed non-collinear. We describe two important cases, spin spirals and skyrmions, and a mathematical concept of topology which characterizes their differences.

Spin spiral

A spin spiral is a periodic non-collinear configuration of spins. The periodicity of the spiral is characterized by its wavevector $\vec{q}$. The wavevector also determines the direction of propagation. A general formula [39] for the direction of the magnetic moment at position $\vec{R}_i$ in a spin spiral is

$$\vec{m}(\vec{R}_i) = \left[\vec{R}_{\vec{q}}\cos\left(\vec{q}\cdot\vec{R}_i\right) + \vec{I}_{\vec{q}}\sin\left(\vec{q}\cdot\vec{R}_i\right)\right]\sin(\theta) \; + \vec{P}_{\vec{q}}\cos(\theta), \tag{1.2}$$

where $\vec{R}_{\vec{q}}$, $\vec{I}_{\vec{q}}$ and $\vec{P}_{\vec{q}}$ are mutually orthogonal and of unit length. The two main type of spin spiral are the conical and the cycloidal spin spirals. For the conical spin spiral, $\vec{P}_{\vec{q}}$ is perpendicular to $\vec{q}$ whereas for the cycloidal spin spiral $\vec{P}_{\vec{q}}$ is parallel to $\vec{q}$. The special case where $\theta = \pi/2$ yields the flat conical and the flat cycloidal spin spirals which are also called Bloch and Néel spin spirals. Fig. 1.5 summarizes the different types of spin spirals.

Topology

Before carrying on with skyrmions, some concepts of topology must be introduced as they are topologically non-trivial magnetic textures.

Two objects are said to be topologically equivalent if one can be continuously transformed into the other. A ball can be continuously deformed into a cube or a cylinder and is therefore topologically equivalent to them. However it is not equivalent to a torus as we would need to pierce a hole in it [34]. In the context of this example we can say that two objects are equivalent if they have the same number of holes or topological charge. A ball, a cube and a cylinder have zero holes and are therefore topologically equivalent. A donut and a cup of coffee both have one hole and are equivalent, etc.

Let us go back to magnetic textures and define their topological charge. In the case of ultrathin magnetic films, the system can be considered as two dimensional and Cartesian coordinates x, y can be used. Let us define the unit magnetization vector $\vec{m}(x,y) = \vec{M}/\left\|\vec{M}\right\|$ with $\vec{M}$ the magnetization. As the norm of $\vec{m}$ is constantly equal to one, $\vec{m}$ is restricted to the unit sphere. The topological charge of a magnetic texture is defined as the number of times $\vec{m}(x,y)$ wraps the unit sphere. Mathematically [34], this is formulated as

$$\begin{aligned} Q &= \frac{1}{4\pi}\int \vec{m}\cdot d\vec{S} \\ &= \frac{1}{4\pi}\int \vec{m}\cdot(\partial_x\vec{m}\times\partial_y\vec{m})dxdy, \end{aligned} \tag{1.3}$$

where we used the shorthand notation $\partial_x = \partial\cdot/\partial x$, $\partial_y = \partial\cdot/\partial y$. A ferromagnetic state and a spin spiral both possess a zero topological charge.

Magnetic skyrmions

Skyrmions are topologically non-trivial spin configurations. They are localized in space and can be viewed as excitations of the ferromagnetic state. They are topologically non-trivial as they posses a non-zero topological charge and therefore cannot be continuously transformed into the ferromagnetic state. Skyrmions can be classified by their topological charge, which is also called winding number. Skyrmions with different topological charges are represented in Fig. 1.6.

The definition of the topological charge from Eq. (1.3) only gives the *total* topological charge of the system. It does not allow us to differentiate magnetic textures with same total topological charge.

To get a better grasp on the topological charge of a skyrmion, let us consider the case of an isolated skyrmion in a ferromagnetic background. Let us use polar coordinates (r,ϕ) for spatial position and spherical angles for the magnetization

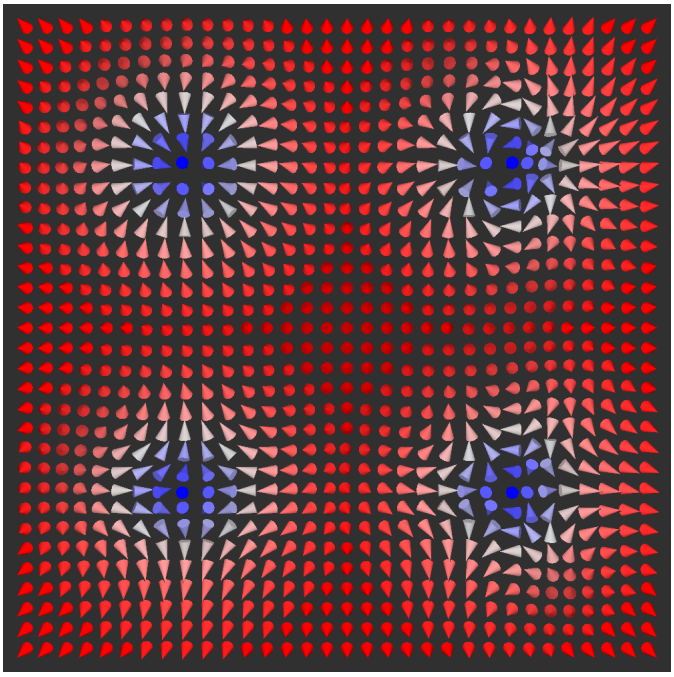

Figure 1.6: Spin lattice configuration corresponding to skyrmions with topological charges of $-1, -2, 1$ and 2 (from left to right, top to bottom).

vector (θ, ψ) with $\theta \in [-\pi/2, \pi/2]$, $\psi \in [-\pi, \pi]$. We assume a spin configuration with radial symmetry such that θ is a function of r only and ψ a function of ϕ only. We can define the vorticity of the skyrmion as

$$n = \frac{1}{2\pi} \int_{-\pi}^{\pi} d\phi \frac{\partial \psi}{\partial \phi}. \tag{1.4}$$

The vorticity represents the net number of (in-plane) rotations of the magnetization along a closed curve encircling the center of the skyrmion. Exploiting the assumption made on θ and ψ, the topological charge can be simplified and reformulated as [34]

$$Q = \frac{n}{2} \left(m_z(0) - m_z(\infty) \right), \tag{1.5}$$

where $m_z(0)$ is the magnetization at the center of the skyrmion ($r = 0$) and $m_z(\infty)$ the asymptotic magnetization far outside the skyrmion ($r \to \infty$).

Before ending this section on magnetic skyrmion, and with it the first chapter, let us take a look at several more complex skyrmionic textures. In Fig. 1.6, we show skyrmions with different topological charge. Systems made up of several skyrmions can also be considered. Fig. 1.7a shows a skyrmionium, which can be viewed as a skyrmion inside a skyrmion and has a zero total topological charge

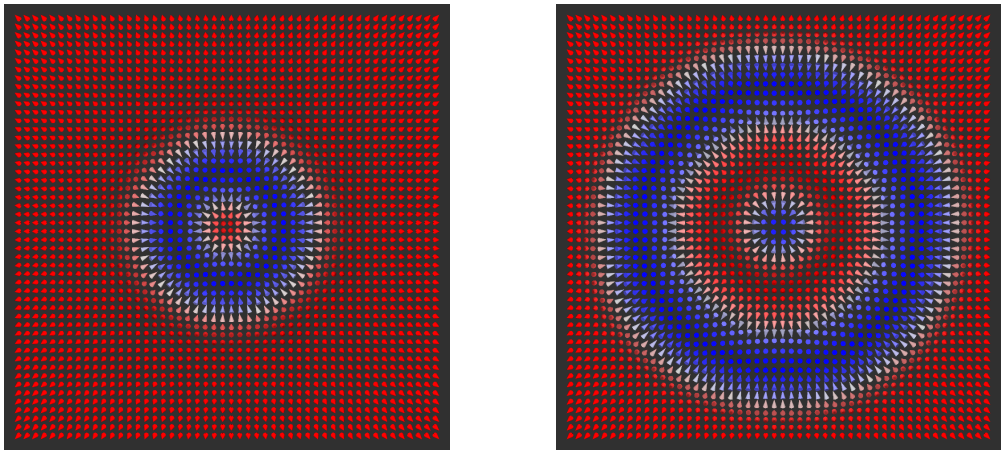

(a) (b)

Figure 1.7: Spin lattice configuration corresponding to a skyrmionium (left) and a target skyrmion (right).

as the two skyrmions have opposite charges. Fig. 1.7b depicts a target skyrmion which is a skyrmion inside a skyrmionium and has a total topological charge of -1. Lastly we have the skyrmion bag which consists of several skyrmions lying inside a skyrmion or a skyrmionium. Its topological charge is, respectively, either equal to the number of skyrmions inside minus one, or equal to minus the number of skyrmions inside.

2 The extended Heisenberg model

This chapter introduces all the required theoretical concepts and tools to study atomistic magnetization dynamics. Firstly, we cover the magnetic Hamiltonian and motivate the choice of Hamiltonian made for this master's thesis. Afterwards we take a look at the modulation of the Dzyaloshinskii-Moriya interaction induced by an external electric field as this modulation plays an important role in the nucleation of skyrmions using an electric field. Finally we cover the governing equations for the time evolution of magnetic textures.

2.1 Magnetic Hamiltonian

As we are concerned with ultrathin films we consider a 2D magnetic lattice. We take z as the out-of-plane component. To each site i of the lattice we associate a magnetic moment $\vec{M}_i$ of constant amplitude $\left\|\vec{M}_i\right\| = \mu_s$. We define the magnetization direction vector as $\vec{m}_i = \vec{M}_i / \left\|\vec{M}_i\right\|$, which is dimensionless.

The magnetic Hamiltonian is generally chosen to be of the form [15]

$$H = H_{\text{Heis}} + H_{\text{ani}} + H_{\text{Zeeman}} + H_{\text{DM}}. \tag{2.1}$$

2.1.1 Exchange interaction

The first term is the Heisenberg exchange interaction. Generally, it is dominant compared to the other terms of the magnetic Hamiltonian. It is written as

$$H_{\text{Heis}} = -\sum_{i,j} J_{ij} \left(\vec{m}_i \cdot \vec{m}_j\right) \tag{2.2}$$

The interaction between first nearest neighbors originates from wavefunction overlap. As electrons are fermionic identical particles, the wavefunction describing a

system of interacting electrons has to be totally antisymmetric [52]. This means that upon the exchange of two electrons the wavefunction must change sign. A consequence of this antisymmetric behavior is that when there is an overlap between the wavefunctions of two electrons the energy of the system is lower (larger) if their spins are antiparallel (parallel). This result in a direct exchange term in the magnetic Hamiltonian.

Beyond first nearest neighbor, the interaction is usually carried by conduction electrons.

In transition metals we have localized d electrons and delocalized s electrons. This gives rise to localized and itinerant magnetism. In the case of an ultrathin film, the s electrons can be treated as a 2 dimensional electron gas (2DEG), whereas the d electrons can be viewed as localized magnetic moments. These localized magnetic moments can interact indirectly via the 2DEG giving rise to an exchange interaction beyond first nearest neighbors. In this case the interaction can be described by the Ruderman–Kittel–Kasuya–Yosida (RKKY) interaction.

When limited to first nearest neighbors, the exchange interaction favors collinear spin configurations. A positive value of J favors a parallel configuration (or ferromagnetic state) whereas a negative J will rather favor an antiparallel configuration (or antiferromagnetic state).

Instead of considering the exchange interaction with all the nearest neighbors, we can limit ourselves to first nearest neighbors by considering an *effective* first nearest neighbor exchange [60]. This effective exchange is tailored in order to account for the beyond nearest neighbors exchange. This is an approximation and does not reproduce all the features of a full treatment (e.g. antiskyrmions are not stable in the effective model) but it greatly reduces the number of parameters for the model.

2.1.2 Magnetic anisotropy energy

The second term in the Hamiltonian is the magnetic anisotropy energy (MAE). It is generally written as

$$H_{\text{ani}} = -K \sum_i \left(\vec{m}_i \cdot \vec{e}_{\text{an}}\right)^2 \tag{2.3}$$

with $\vec{e}_{\text{an}}$ the axis of anisotropy. Higher order terms ($(\vec{m}_i \cdot \vec{e}_{\text{an}})^4$,...) can be included but they are generally of lesser significance. When $K > 0$ the anisotropic axis is said to be an easy axis as the magnetization along this axis is favored. In the opposite case, when $K < 0$, we have an hard axis, or easy plane, of magnetization and a magnetization contained within the plane perpendicular to the hard axis is favored. For ultrathin films the anisotropic axis is generally the z-axis and the

anisotropy energy term can be rewritten as

$$H_{\text{ani}} = -K \sum_i m_{i,z}^2 \tag{2.4}$$

with $m_{i,z}$ the z-component of $\vec{m}_i$.

There are two contributions included in the MAE: the magnetocrystalline anisotropy and the dipole-dipole coupling between magnetic moments.

Magnetocrystalline anisotropy

The magnetocrystalline anisotropy originates from spin-orbit coupling. The spins are coupled to the crystal lattice. This has as consequence that some crystallographic axes are more favorable than others. For a single principal axis, which is generally the case for ultrathin films, it can readily be modeled by Eq. (2.4). In the case of cubic crystal structures (e.g. bulk iron or nickel), there are three principal axis [16] and the anisotropy is rather modeled by

$$H_{\text{ani}}^{\text{cub}} = -K^{\text{cub}} \sum_i (m_{i,x}^4 + m_{i,y}^4 + m_{i,z}^4). \tag{2.5}$$

As the magnetocrystalline anisotropy originates from SOC, it is particularly important if heavy elements are present.

Dipole-dipole interaction

The second contribution included in the MAE is the dipole-dipole interaction between the magnetic moments. The dipole-dipole interaction energy can be computed from classical magnetostatics and is given by [15]

$$H_{\text{dd}} = -\frac{\mu_0 \mu_s^2}{4\pi} \sum_{i,j} \frac{1}{r_{ij}^3} \left(3(\vec{m}_i \cdot \hat{r}_{ij})(\vec{m}_j \cdot \hat{r}_{ij}) - \vec{m}_i \cdot \vec{m}_j\right), \tag{2.6}$$

where $\hat{r}_{ij}$ is the unit vector going from site i to site j and r_{ij} the distance between the two. This is a long range interaction and can be computationally intensive. In thin films, it can be seen as a shape anisotropy which favors an in-plane orientation of the magnetization. This shape anisotropy can be formally accounted for by an effective magnetic anisotropy of the form of Eq. (2.4) [42].

2.1.3 Zeeman energy

The third term in the Hamiltonian is the Zeeman energy and takes the form

$$H_{\text{Zeeman}} = -\sum_i \mu_s \vec{m}_i \cdot \vec{B}_i \tag{2.7}$$

where $\vec{B}_i$ is the external magnetic field at site i. It arises from the interaction of the magnetic moments with the magnetic field.

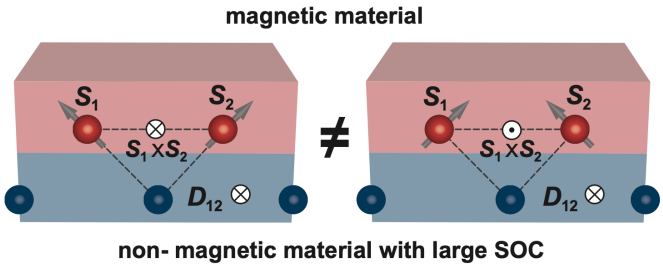

Figure 2.1: Degeneracy lifting between spin spirals rotating in opposite direction in ultrathin films. The left configuration is energitically more favorable (from Eq. (2.8)). Figure taken from Ref. [39].

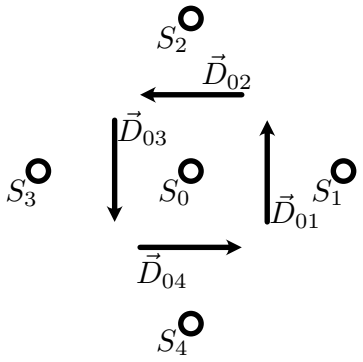

Figure 2.2: Depiction of the direction of the DM vectors in the case of a square lattice.

2.1.4 Dzyaloshinskii-Moriya interaction

The last term in the magnetic Hamiltonian is the Dzyaloshinskii-Moriya interaction (DMI/DM interaction) [14, 41]. It is an antisymmetric indirect exchange between two magnetic moments caused by a third non-magnetic atom. It is written as

$$H_{\mathrm{DM}} = -\sum_{ij} \vec{D}_{ij} \cdot (\vec{m}_i \times \vec{m}_j)\,. \tag{2.8}$$

The vector $\vec{D}_{ij}$ is called the DM vector and we have $\vec{D}_{ij} = -\vec{D}_{ji}$. Generally, only the interaction between two nearest neighbors is taken into account as it is already an order of magnitude smaller than the Heisenberg exchange. It favors non-collinear configurations. It also brings chirality to the system. Without DMI, left- and right-rotating spin spirals are degenerate in energy. The DM interaction lifts this degeneracy as it favors one over the other. This is visually explicited in Fig. 2.1 in the case of an ultrathin film.

This interaction originates from SOC caused by the third atom in the presence

of an inversion asymmetry and is carried by conduction electrons in transition metals. It can also originate from wavefunction overlap (in the presence of SOC as well) as it is the case for α-Fe_2O_3 [41]. In the case where the DM interaction is transferred via a single third atom, let $\vec{R}_i$ (resp. $\vec{R}_j$) be the vector going from site i (resp. j) to this third atom. Then the DM vector will be in the direction of $\vec{R}_i \times \vec{R}_j$ [30, 10].

The required inversion asymmetry can either be due to a bulk inversion asymmetry or due to an interface. They give rise to a bulk DMI or an interfacial DMI respectively. Regarding the interfacial DMI, Crépieux and Lacroix [11] determined the direction of the DM vector for several systems. In the case of a square magnetic lattice, the DM vectors are represented in Fig. 2.2. The DM vectors are contained in the plane of the interface and perpendicular to the vector joining the two spins. Mathematically, the direction of the DM vector $\vec{D}_{ij}$ is given by

$$\vec{D}_{ij} = D_{ij}\hat{z} \times \hat{r}_{ij} \tag{2.9}$$

where $\hat{z}$ is the unit normal to the interface.

2.2 Dzyaloshinskii-Moriya interaction induced by an external electric field

In this section we will describe how an electric field can induce a DM-like interaction in ultrathin metallic films. This section is a summarized version of the first part of *Desplat et al.* [12].

The application of an external electric field $\vec{E}_{\text{ext}}$ induces an internal electric field $\vec{E}_{\text{int}}$ inside the ultrathin film, proportional to the external field. The total electric field generates a Rashba spin-orbit coupling (SOC) among the 2DEG formed by the conduction electrons:

$$H_{\text{SOC}} = \frac{e\hbar}{4mc^2}\vec{\sigma} \cdot \left(\left(\vec{E}_{\text{ext}} + \vec{E}_{\text{int}}\right) \times \vec{p}\right) \tag{2.10}$$

$$\propto \vec{\sigma} \cdot \left(\vec{E}_{\text{ext}} \times \vec{p}\right), \tag{2.11}$$

with $\vec{\sigma}$ the vector of Pauli matrices and $\vec{p}$ the electron momentum. Starting from here, we switch to the shorter notation $\vec{E}$ for the external electric field. The Rashba SOC influences the RKKY interaction between localized spins which gives rise to a DM-like interaction [26] which is of the form

$$H_{\text{ME}} = -\sum_i \sum_{j \in NN_i} \vec{D}_{ij}^{\text{ME}} \cdot (\vec{m}_i \times \vec{m}_j) \tag{2.12}$$

with the magnetoelectric DM vector

$$\vec{D}_{ij}^{\mathrm{ME}} = \alpha_{\mathrm{ME}} \left(\vec{E} \times \hat{r}_{ij} \right). \tag{2.13}$$

We call α_{ME} the magnetoelectric coupling constant. For 3d transition-metal monolayers, this constant is usually on the order of 10^{15} eVm/V [12]. We can formulate an effective DM interaction by summing the pre-existing DMI and the induced one:

$$H_{\mathrm{DM,eff}} = -\sum_i \sum_{j \in NN_i} \left[\vec{D}_{ij} + \alpha_{\mathrm{ME}} \left(\vec{E} \times \hat{r}_{ij} \right) \right] \cdot (\vec{m}_i \times \vec{m}_j) \tag{2.14}$$

$$= -\sum_i \sum_{j \in NN_i} \vec{D}_{ij}^{\mathrm{eff}} \cdot (\vec{m}_i \times \vec{m}_j) \tag{2.15}$$

with $\vec{D}_{ij}^{\mathrm{eff}}$ the effective DM vector. This allows the modulation of the direction and intensity of the DM interaction.

In the case of an electric field directed along the z direction, the effective DMI on a square lattice can be reformulated as

$$\vec{D}_{ij}^{\mathrm{eff}} = (D_{ij} + \alpha_{\mathrm{ME}} E)\, \hat{z} \times \hat{r}_{ij} \tag{2.16}$$

where we used Eq. (2.9) for the expression of the interfacial DMI on a square lattice. The induced DMI is of the same form as the interfacial DMI, which is intrinsic to the material. This permits the modulation of the DM interaction in intensity only.

2.3 Time evolution of the magnetic textures

In this section we will first cover the equation of motion for quantum mechanical spins. The obtained equation then serves as a basis for the derivation of the equation of motion for classical magnetic moments.

2.3.1 Spin dynamics

We start from Pauli's equation [51] for the electron

$$i\hbar \partial_t \psi = \hat{H}\psi \; = \left(\frac{1}{2m} \left(\hat{\vec{p}} - q\vec{A} \right)^2 + q\phi - \frac{q\hbar}{2m} \hat{\vec{\sigma}} \cdot \vec{B} \right) \psi, \tag{2.17}$$

where $\psi = \begin{pmatrix} \psi_+ & \psi_- \end{pmatrix}$ is the electron spinor, $\vec{A}$ the magnetic vector potential, ϕ the electric scalar potential, $q = -e$ is the charge of the electron and $\hat{\vec{\sigma}}$ is the vector of Pauli matrices. In index notation the Hamiltonian reads as

$$\hat{H}_{\alpha\beta} = \left(\frac{1}{2m} \left(\hat{\vec{p}} - q\vec{A} \right)^2 + q\phi \right) \delta_{\alpha\beta} - \frac{q\hbar}{2m} \hat{\sigma}_{j\alpha\beta} B_j. \tag{2.18}$$

The expectation value for the spin is defined as

$$\langle \vec{s} \rangle = \psi^* \hat{\vec{s}} \psi = \frac{1}{2} \psi^* \hat{\vec{\sigma}} \psi. \tag{2.19}$$

Its time evolution is given through its commutator with the Hamiltonian by

$$\partial_t \langle \vec{s} \rangle = \frac{1}{2i\hbar} \psi^* [\hat{\vec{\sigma}}, \hat{H}] \psi. \tag{2.20}$$

In index notation we have

$$\partial_t \langle s_i \rangle = \frac{1}{2i\hbar} \psi^*_\alpha [\hat{\sigma}_i, \hat{H}]_{\alpha\beta} \psi_\beta. \tag{2.21}$$

From (2.18), the commutator of $\hat{\sigma}_i$ and the first term of the Hamiltonian is zero. For the commutator with the second term, let us recall that $[\hat{\sigma}_i, \hat{\sigma}_j]_{\alpha\beta} = 2i\epsilon_{ijk}\hat{\sigma}_{k\alpha\beta}$. The time evolution is given by

$$\partial_t \langle s_i \rangle = -\frac{q}{2m} \psi^*_\alpha \epsilon_{ijk} B_j \hat{\sigma}_{k\alpha\beta} \psi_\beta \tag{2.22}$$

$$= \frac{q}{2m} \psi^*_\alpha (\hat{\vec{\sigma}}_{\alpha\beta} \times \vec{B})_i \psi_\beta \tag{2.23}$$

$$\Rightarrow \partial_t \langle \vec{s} \rangle = -|\gamma_e| \langle \vec{s} \rangle \times \vec{B}, \tag{2.24}$$

with $\gamma_e = q/m = -e/m$ the gyromagnetic ratio of the electron. Under the application of a constant magnetic field the expectation value for the spin will start to precess around the magnetic field.

2.3.2 Magnetization dynamics

The Landau-Lifshitz-Gilbert equation (LLG) [15] describes the time evolution of magnetic moments and can be written as

$$\frac{\partial \vec{m}_i}{\partial t} = -\frac{\gamma}{\mu_s} \vec{m}_i \times \vec{B}_{i,\text{eff}} - \alpha_{\text{LLG}} \frac{\gamma}{\mu_s} \vec{m}_i \times \frac{\partial \vec{m}_i}{\partial t} \tag{2.25}$$

with γ the gyromagnetic ratio, $\vec{B}_{i,\text{eff}}$ the local effective magnetic field and α_{LLG} the dimensionless damping parameter. It is similar to Eq. (2.24), to which a phenomenological damping term was added by Gilbert [21]. The damping term was added in order to account for the observation that magnetic moments in an external magnetic field do not precess indefinitely but eventually align with the external field. The motivation for the form of the damping term originates from classical mechanics: classically a particle moving through a viscous medium experiences a drag force proportional to its velocity and opposite in direction.

The Landau-Lifshitz-Gilbert equation can be reformulated as

$$\frac{\partial \vec{m}_i}{\partial t} = -\frac{\gamma_L}{\mu_s}\vec{m}_i \times \vec{B}_{i,\text{eff}} - \alpha_{\text{LLG}}\frac{\gamma_L}{\mu_s}\vec{m}_i \times \left(\vec{m}_i \times \vec{B}_{i,\text{eff}}\right) \tag{2.26}$$

where $\gamma_L = \gamma/(1+\alpha_{\text{LLG}}^2)$ is the renormalized gyromagnetic ratio. The first term on the right hand side of the equation will cause the magnetic moment to precess around $\vec{B}_{i,\text{eff}}$ and is energy conserving. The second term is responsible for dissipation and will bring $\vec{m}_i$ to align with $\vec{B}_{i,\text{eff}}$.

With H the magnetic Hamiltonian (as defined in Eq. (2.1)), the effective magnetic field $\vec{B}_{i,\text{eff}}$ at site i is given by

$$\vec{B}_{i,\text{eff}} = -\frac{\partial H}{\partial \vec{m}_i}. \tag{2.27}$$

This effective field takes into account the external applied magnetic field as well as the interaction of the magnetic moment with its neighbors and with the external electric field. The numerical time integration of Eq. (2.26) will allow us to study the dynamical nucleation of skyrmions. All the magnetization dynamics carried throughout this master's thesis were performed using the Matjes code[1] developed by Dr. Bertrand Dupé within the Nanomat group.[2]

2.3.3 Magnetization dynamics for laser pulses

The Landau-Lifshitz-Gilbert equation used in combination with the magnetic Hamiltonian enables us to model the time evolution of magnetic textures under the application of a laser pulse. The laser pulse acts upon the magnetic texture via the modulation of the DMI by its electric field (see Eq. (2.13)), and via the Zeeman term in the Hamiltonian through its magnetic field.

Non-uniform time-dependent fields can be considered. Naturally, these should obey Maxwell's equation. We decided to use Laguerre-Gauss beams as they are monochromatic solutions to Maxwell's equations, have finite spatial extension and carry orbital angular momentum (OAM). Our main interest in Laguerre-Gauss beams lies in their OAM as we aim to transfer angular momentum to the magnetic system in a controllable way and nucleate topological magnetic texture. The LG beams will be the main subject of the next chapter.

In chapter 4, we perform magnetization dynamics simulation on a square lattice with the particular case of beams with an electric field directed along the z direction. Using Eq. (2.16) for the expression of the effective DMI, we can already

[1] https://github.com/bertdupe/Matjes
[2] http://www.nanomat.ulg.ac.be/

particularize the expression of the magnetic Hamiltonian (2.1) for this case:

$$\begin{aligned} H =& H_{\text{Heis}} + H_{\text{ani}} + H_{\text{Zeeman}} + H_{\text{DM,eff}} \\ =& -\sum_i \sum_{j \in NN} J \vec{m}_i \cdot \vec{m}_j - \sum_i K m_{i,z}^2 - \sum_i \mu_s \vec{m}_i \cdot \vec{B}_i \\ & - \sum_i \sum_{j \in NN} (D + \alpha_{\text{ME}} E) \left(\hat{z} \times \hat{r}_{ij} \right) \cdot \left(\vec{m}_i \times \vec{m}_j \right). \end{aligned} \tag{2.28}$$

We use an effective first nearest neighbor exchange as well.

3

Theory on Laguerre-Gauss beams

Laguerre-Gauss beams are electromagnetic waves carrying orbital angular momentum. They are therefore able to transfer angular momentum to the spin lattice. This transfer may help reduce the amount of energy needed for the nucleation. These symmetries may also enable the nucleation of topologically non-trivial structures such as skyrmions but also target skyrmions, skyrmion bags and higher order skyrmions.

As they are electromagnetic waves, they are composed of an electric field and a magnetic field. The main steps to derive the shape of the electric field are detailed in the first section of this chapter. A more in-depth derivation can be found in references [47, 19]. In the second section, we will derive the expression of the magnetic field. This derivation is a result of this thesis. This derivation was not found in the specialized references consulted for the derivation of the electric field and had to be carried out from scratch. LG beams were also implemented in the Matjes code, used for the spin dynamics simulation, as part of this master's thesis.

As a matter of reference, we will recall Maxwell's equations formulated in vacuum in the absence of charges/currents (in SI units):

$$\nabla \cdot \vec{E} = 0, \tag{3.1}$$

$$\nabla \cdot \vec{B} = 0, \tag{3.2}$$

$$\nabla \times \vec{E} = -\frac{\partial}{\partial t}\vec{B}, \tag{3.3}$$

$$\nabla \times \vec{B} = \varepsilon_0 \mu_0 \frac{\partial}{\partial t}\vec{E}. \tag{3.4}$$

3.1 Electric field

The starting point of the derivation is the wave equation:

$$\partial_{tt}\vec{E} - \varepsilon_0\mu_0\nabla^2\vec{E} = 0, \tag{3.5}$$

where we used the shorthand notation $\partial_{tt}\cdot = \partial^2\cdot/\partial t^2$. The wave equation can readily be derived from Maxwell's equations. Since each component of the electric field obeys the wave equation independently from the others, we can solve the equation for one component only, i.e. solving $\partial_{tt}E_i - \varepsilon_0\mu_0\nabla^2 E_i = 0$, with $i = x, y, z$. Searching for a monochromatic wave propagating in the $+z$ direction the electric field is of the form

$$E_i(x,y,z,t) = \mathscr{E}_i(x,y,z)e^{-i(\omega t-kz)} + \mathscr{E}_i^*(x,y,z)e^{i(\omega t-kz)} \tag{3.6}$$

with $\omega = 2\pi/T = kc$, c being the speed of light in vacuum. Inserting this expression in the wave equation, we get

$$\left(\partial_{xx} + \partial_{yy} + \partial_{zz} + 2ik\partial_z\right)\mathscr{E}_i = 0. \tag{3.7}$$

Within the paraxial approximation we consider that the electric field varies much more rapidly along x and y than along z. Therefore the term in ∂_{zz} is ignored and we obtain the paraxial wave equation

$$\left(\partial_{xx} + \partial_{yy} + 2ik\partial_z\right)\mathscr{E}_i = 0. \tag{3.8}$$

This equation can be solved by separation of variables either in Cartesian or in cylindrical coordinates giving rise to the Hermite-Gauss modes and the Laguerre-Gauss modes respectively. Each type of modes forms a family of solution that can be indexed by two integers which are usually denoted m, n for Hermite-Gauss and l, p for Laguerre-Gauss, with m, n and p being non-negative integers. The Hermite-Gauss modes are given by

$$\mathscr{E}^{\mathrm{HG}}_{m,n}(x,y,z) = \frac{\mathscr{E}^{\mathrm{HG}}_{0(m,n)}}{w(z)} H_m\left(\frac{x\sqrt{2}}{w(z)}\right) H_n\left(\frac{y\sqrt{2}}{w(z)}\right) e^{-\frac{r^2}{w^2(z)}} e^{i\psi(z)} \tag{3.9}$$

and the Laguerre-Gauss modes by

$$\mathscr{E}^{\mathrm{LG}}_{l,p}(r,\phi,z) = \frac{\mathscr{E}^{\mathrm{LG}}_{0(l,p)}}{w(z)} \left(\frac{r\sqrt{2}}{w(z)}\right)^{|l|} L_p^{|l|}\left(\frac{2r^2}{w^2(z)}\right) e^{-\frac{r^2}{w^2(z)}} e^{i\frac{kr^2}{2R}} e^{i[l\phi-(2p+|l|+1)\psi(z)]} \tag{3.10}$$

where H_m and $L_p^{|l|}$ are Hermite and generalized Laguerre polynomials respectively. We introduced several quantities:

- the Rayleigh range $z_R = \frac{kw_0^2}{2}$,
- the beam size $w(z) = w_0\sqrt{1 + \left(\frac{z}{z_R}\right)^2}$, with w_0 the size of the beam at the waist,
- the radius of curvature of the wavefront $R(z) = z\left(1 + \left(\frac{z_R}{z}\right)^2\right)$,
- and the Gouy phase $\psi(z) = \arctan\left(\frac{z}{z_R}\right)$.

For $z = 0$ the beam size is minimal and equal to w_0 and the wavefront is planar as $R \to \infty$.

The factors $\mathscr{E}^{\mathrm{HG}}_{0(m,n)}$ and $\mathscr{E}^{\mathrm{LG}}_{0(l,p)}$ are normalization factors and are given by

$$\mathscr{E}^{\mathrm{HG}}_{0(m,n)} = \frac{1}{\sqrt{2^n n!}}\left(\frac{2}{\pi}\right)^{1/4}, \tag{3.11}$$

$$\mathscr{E}^{\mathrm{LG}}_{0(l,p)} = \sqrt{\frac{2^{|l|+1}p!}{\pi(p+|l|)!}}. \tag{3.12}$$

Each family of solutions forms a complete basis of orthogonal functions. Therefore any Laguerre-Gauss mode can always be viewed as a superposition of Hermite-Gauss modes and vice versa.

We will now put aside the Hermite-Gauss modes as our main interest lies in the Laguerre-Gauss modes as they carry angular momentum (which Hermite-Gauss modes do not). The spatial distribution and time evolution of lowest order Laguerre-Gauss modes are represented in Fig. 3.1 and 3.2. The absolute value of l dictates the number of nodes and anti-nodes along the azimuthal direction whereas p dictates the number of nodes and anti-nodes along the radial direction. Therefore we will call l the azimuthal number and p the radial number. Furthermore the electric field seems to "rotate" counter-clockwise for modes with a strictly positive azimuthal number. For negative values of l, the rotation would be clockwise.

At the beginning of the section we mentioned that each component of the electric field obeys the wave equation independently and we chose to solve it for one component. Therefore in the most general case each component of the electric field is a superposition of Laguerre-Gauss modes. In the context of this master's thesis we will consider electric fields whose z component is the sole non-zero one (the x and y components are set to zero). The electric field is consequently of the form

$$\vec{E} = \left(\mathscr{E}^{\mathrm{LG}}_{l,p}e^{-i(\omega t - kz)} + \mathscr{E}^{\mathrm{LG}^*}_{l,p}e^{i(\omega t - kz)}\right)\hat{z}. \tag{3.13}$$

This choice was initially motivated by the encouraging results obtained by *Desplat et al.* [12] with a pulsed electric field directed along z. Such an electric field induces

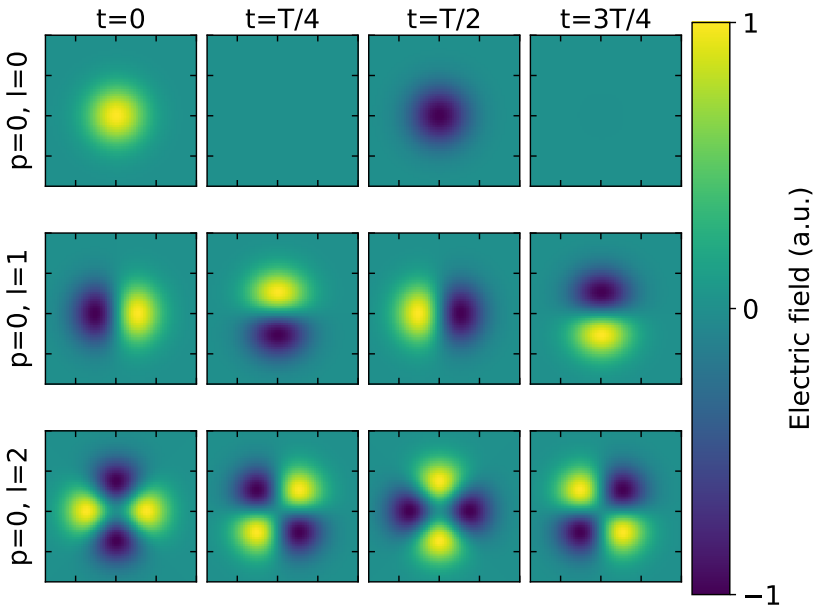

Figure 3.1: Spatial distribution and time evolution of the electric field for Laguerre-Gauss modes with $p = 0$ in the xy-plane at $z = 0$.

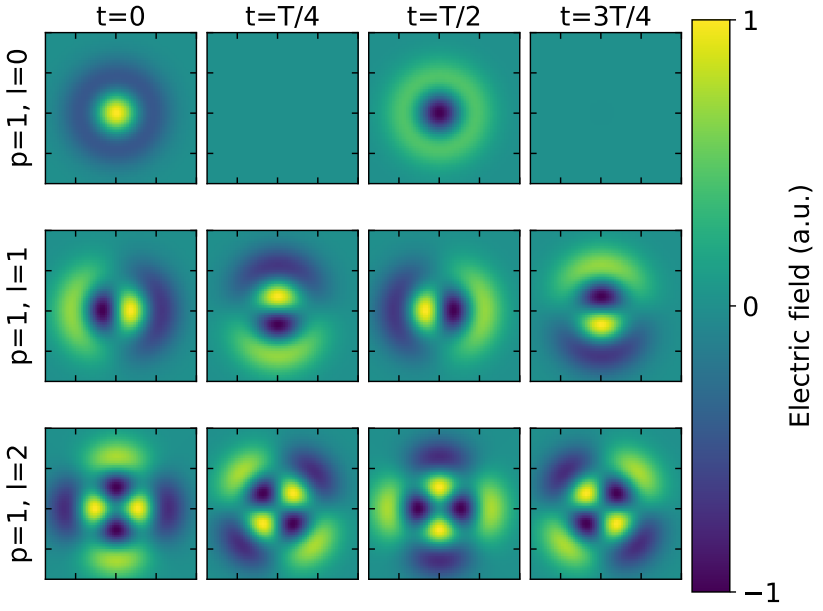

Figure 3.2: Spatial distribution and time evolution of the electric field for Laguerre-Gauss modes with $p = 1$ in the xy-plane at $z = 0$.

a DMI interaction whose DM vector is in-plane. This induced DMI is similar to the already existing interfacial DMI for a square lattice so that it modulates only the norm of the effective DM vector and not its direction (as already seen in the previous chapter, see section 2.2).

3.2 Magnetic field

We now take a look at the magnetic field of the Laguerre-Gauss beam. The magnetic field should obey Maxwell's equations and be consistent with the electric field we found in the last section. To derive a solution for the magnetic field starting from the electric field we could use either Eq. (3.3) or (3.4). If we re-inject the magnetic field obtained using either equation in the other equation, this would yield back the original electric field.

For simplicity we will use (3.3) (Faraday's law). Considering Eq. (3.13), we have

$$\begin{aligned}\vec{\nabla}\times\vec{E} &= \vec{\nabla}\times(E\hat{z}) \\ &= \frac{1}{r}\frac{\partial E}{\partial\phi}\hat{r} - \frac{\partial E}{\partial r}\hat{\phi} \\ &= -\frac{\partial\vec{B}}{\partial t}.\end{aligned} \tag{3.14}$$

Therefore the magnetic field is entirely in-plane and can be written as $\vec{B} = B_r\hat{r} + B_\phi\hat{\phi}$. Furthermore the magnetic field should be of the same form as Eq. 3.6 and we have

$$B_r(x,y,z,t) = \mathscr{B}^{\mathrm{LG}}_{r,(l,p)}e^{-i(\omega t-kz)} + \left(\mathscr{B}^{\mathrm{LG}}_{r,(l,p)}\right)^* e^{i(\omega t-kz)}, \tag{3.15}$$

$$B_\phi(x,y,z,t) = \mathscr{B}^{\mathrm{LG}}_{\phi,(l,p)}e^{-i(\omega t-kz)} + \left(\mathscr{B}^{\mathrm{LG}}_{\phi,(l,p)}\right)^* e^{i(\omega t-kz)}. \tag{3.16}$$

In order to lighten the notation, we will simply write $\mathscr{E}^{\mathrm{LG}}_z$, $\mathscr{B}^{\mathrm{LG}}_{r,(l,p)}$ and $\mathscr{B}^{\mathrm{LG}}_{\phi,(l,p)}$ as $\mathscr{E}$, $\mathscr{B}_r$ and $\mathscr{B}_\phi$. Eq. (3.14) becomes

$$\frac{1}{r}\frac{\partial\mathscr{E}}{\partial\phi} = i\omega\mathscr{B}_r, \tag{3.17}$$

$$-\frac{\partial\mathscr{E}}{\partial r} = i\omega\mathscr{B}_\phi. \tag{3.18}$$

For the radial component we get

$$\begin{aligned}\mathscr{B}_r &= \frac{l}{r\omega}\mathscr{E} \\ &= \frac{l}{r\omega}\frac{\mathscr{E}^{\mathrm{LG}}_{0(l,p)}}{w(z)}\left(\frac{r\sqrt{2}}{w(z)}\right)^{|l|} L_p^{|l|}\left(\frac{2r^2}{w^2(z)}\right)e^{-\frac{r^2}{w^2(z)}}e^{i\frac{kr^2}{2R}}e^{i(l\phi-(2p+|l|+1)\psi(z)}\end{aligned} \tag{3.19}$$

and for the azimuthal one

$$\begin{aligned}\mathscr{B}_\phi =&\mathscr{E}_0\frac{\sqrt{2}^{|l|}}{w^{|l|+1}}\left[\frac{i|l|}{\omega}r^{|l|-1}L_p^{|l|}\left(\frac{2r^2}{w^2}\right)-\frac{i}{\omega}\frac{4r^{|l|+1}}{w^2}L_{p-1}^{|l|+1}\left(\frac{2r^2}{w^2}\right)\right.\\&\left.-\frac{i}{\omega}\frac{2r^{|l|+1}}{w^2}L_p^{|l|}\left(\frac{2r^2}{w^2}\right)-\frac{1}{Rc}r^{|l|+1}L_p^{|l|}\left(\frac{2r^2}{w^2}\right)\right]\\&\cdot e^{-\frac{r^2}{w^2}}e^{i\frac{kr^2}{2R}}e^{i[l\phi-(2p+|l|+1)\psi(z)]}.\end{aligned}\tag{3.20}$$

Injecting these results in Eq. (3.15) and (3.16) and recombining the complex exponentials in sine and cosine, one obtains

$$B_r=\frac{2l}{r\omega}\frac{\mathscr{E}^{\mathrm{LG}}_{0(l,p)}}{w(z)}\left(\frac{r\sqrt{2}}{w(z)}\right)^{|l|}L_p^{|l|}\left(\frac{2r^2}{w^2(z)}\right)e^{-\frac{r^2}{w^2(z)}}\cos\left(kz-\omega t+\varphi\right),\tag{3.21}$$

and

$$\begin{aligned}B_\phi=&-\frac{2|l|}{\omega}\mathscr{E}^{\mathrm{LG}}_{0(l,p)}\frac{r^{|l|-1}\sqrt{2}^{|l|}}{w^{|l|+1}}L_p^{|l|}\left(\frac{2r^2}{w^2}\right)e^{-\frac{r^2}{w^2}}\sin(kz-\omega t+\varphi)\\&+\frac{8}{\omega}\mathscr{E}^{\mathrm{LG}}_{0(l,p)}\frac{r^{|l|+1}\sqrt{2}^{|l|}}{w^{|l|+3}}L_{p-1}^{|l|+1}\left(\frac{2r^2}{w^2}\right)e^{-\frac{r^2}{w^2}}\sin(kz-\omega t+\varphi)\\&+\frac{4}{\omega}\mathscr{E}^{\mathrm{LG}}_{0(l,p)}\frac{r^{|l|+1}\sqrt{2}^{|l|}}{w^{|l|+3}}L_p^{|l|}\left(\frac{2r^2}{w^2}\right)e^{-\frac{r^2}{w^2}}\sin(kz-\omega t+\varphi)\\&-\frac{2}{Rc}\mathscr{E}^{\mathrm{LG}}_{0(l,p)}\frac{r^{|l|+1}\sqrt{2}^{|l|}}{w^{|l|+1}}L_p^{|l|}\left(\frac{2r^2}{w^2}\right)e^{-\frac{r^2}{w^2}}\cos(kz-\omega t+\varphi),\end{aligned}\tag{3.22}$$

with

$$\varphi=\frac{kr^2}{2R}+l\phi-(2p+|l|+1)\,\psi(z).\tag{3.23}$$

We see that the beam rotates around its center at an angular speed of ω/l. This result can be obtained by taking the time derivative of the argument of the sine/cosine functions and setting it to zero.[1] This has as a consequence that a beam with a larger value l will rotate slower.

The shape of the lowest order modes in the xy-plane at the beam waist at time $t=T/4$ are represented in Fig. 3.3 and 3.4. We see that the magnetic field forms closed loops. This is in accordance with the fact that the magnetic field has a zero divergence. By comparing these figures with those of the electric field (Figs. 3.1

[1]This result could have already been obtained from the expression of the electric field but would have probably been less obvious as its expression was not re-expressed in terms of sine/cosine functions.

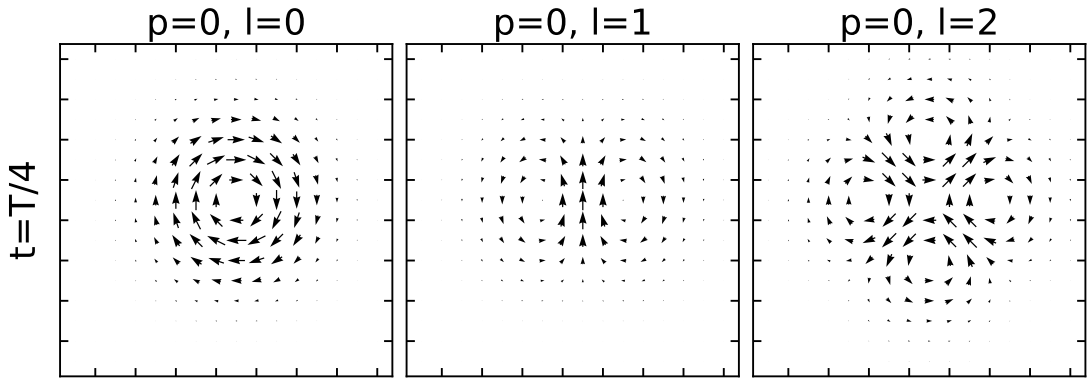

Figure 3.3: Spatial distribution at $t = T/4$ of the magnetic field for Laguerre-Gauss modes with $p = 0$ in the xy-plane at $z = 0$.

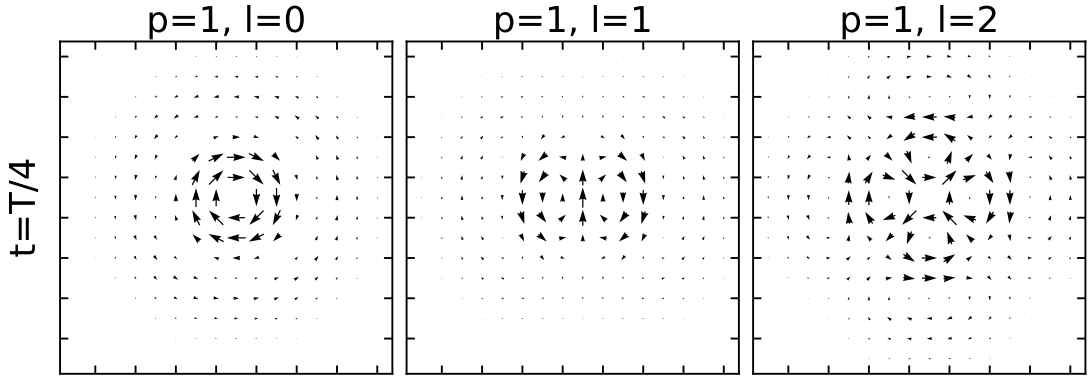

Figure 3.4: Spatial distribution at $t = T/4$ of the magnetic field for Laguerre-Gauss modes with $p = 1$ in the xy-plane at $z = 0$.

and 3.2), we also see that the closed loops encircle the anti-nodes of the electric field. For non-zero values of l the closed loops will rotate around the center of the beam in the same way as the electric field.

4 Results

In chapter 2 we covered the theory regarding the magnetic Hamiltonian and magnetization dynamics, applied to laser pulses. Afterwards, Laguerre-Gauss beams were explained in chapter 3, including a derivation of the analytical expressions of the electric and magnetic fields. In this chapter we present the results obtained throughout this master's thesis as well as the development made to obtain these results.

This chapter is divided in 3 parts. First, we describe an algorithm for the identification of skyrmionic textures. The aim of this algorithm is the automatic treatment of simulation results. Afterwards, in the second part, we explore the nucleation of single skyrmions via an external electric field. Then we consider Laguerre-Gauss beams in the last part.

4.1 Automatic identification of skyrmions

In this section we will describe an algorithm for the identification of skyrmions. We can readily compute the total topological charge of the whole magnetic system using Eq. (1.3). However this does not allow to differentiate a target skyrmion from a simple skyrmion, or a skyrmion with a charge of -2 from two individual skyrmions with a charge of -1 each. Regarding the current state of the art, most of the effort on the subject is focused on either the determination of the magnetic phase (ferromagnetic, skyrmion lattice, spin spiral) [25, 53, 2] or the counting of skyrmions in a system [38]. All works make use of machine learning or neural networks. As far as I am aware, no works has yet been carried out towards the identification of complex skyrmionic textures such as higher order skyrmions, target skyrmions, etc. The algorithm presented here is able to reliably identify such textures.

There are two requirements on the use of this algorithm. The first one is

that we must have a ferromagnetic background. Therefore it will not work for antiferromagnetic skyrmions but could easily be modified for that purpose. It could also be modified in order to work with half integer topological magnetic textures. The second requirement is that the magnetization must be relaxed. This requirement does not allow for the dynamical identification of skyrmions.

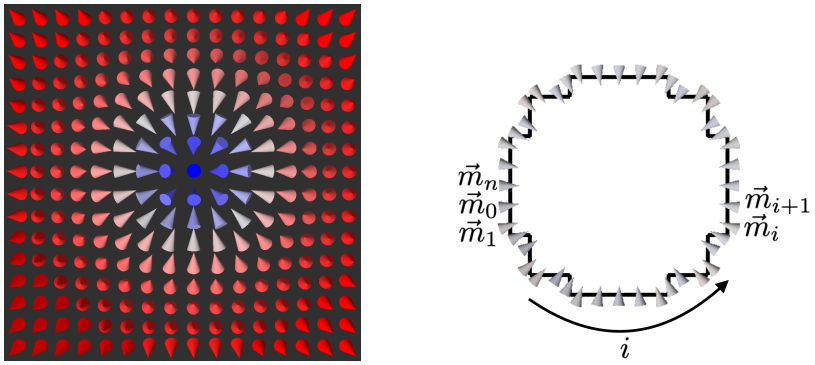

(a) Spin lattice (b) Skyrmion contour

Figure 4.1: Detection of the contour of a skyrmion starting from the spin lattice. The magnetic moments forming the forming the contour should be ordered such as to run over the contour counterclockwise.

The first step is to identify the contour of the skyrmions' core. We define the contour of a skyrmion's core as the set of points where the z-component of the magnetization changes sign (i.e. where it goes through zero) and the core as the region inside. In order to identify the contours, we go through the lattice from left to right and from bottom to top and detect whenever m_z changes sign. Fig. 4.1 shows the contour of a skyrmion as identified by the algorithm.

Once the contours are determined, we compute the topological charge associated to each. Let $(\vec{m}_i)_{i\in\{0,\dots,n\}}$ be the indexed set of magnetic moments forming a contour, as depicted in Fig. 4.1b. The magnetic moments are indexed so as to run over the contour counterclockwise. Using spherical angles to represent the magnetic moments, we denote by θ_i and ψ_i the polar and azimuthal angles associated to $\vec{m}_i$ with $\theta_i \in [-\pi/2, \pi/2]$, $\psi_i \in [-\pi, \pi]$. We discretize the definition of the vorticity (as defined in Eq. (1.4))

$$n = \frac{1}{2\pi} \sum_{i}^{n} f(\psi_{i+1} - \psi_i). \tag{4.1}$$

The function f essentially brings any angle back to the interval $[-\pi, \pi]$ and is defined as

$$f(x) = [(x + \pi) \mod 2\pi] - \pi. \tag{4.2}$$

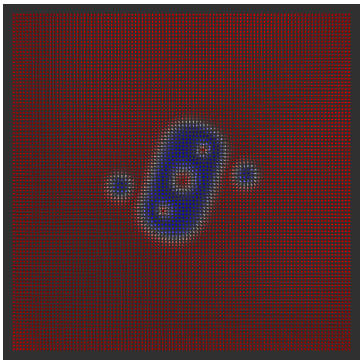

(a) Spin lattice

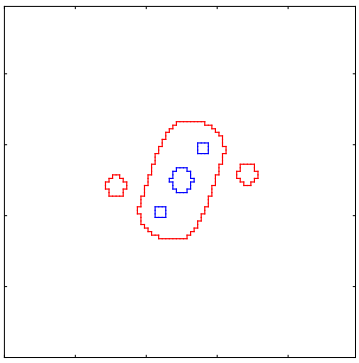

(b) Skyrmion contours: blue curves have a charge of 1 an the red ones a charge of -1

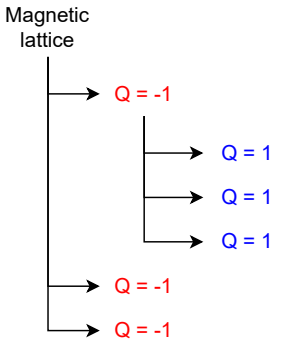

(c) Tree structure representation

Figure 4.2: Demonstration example of automatic identification of skyrmionic textures.

This enables us to compute the topological charge of each contour.

The next step is to determine whether or not a skyrmion is comprised within another, as it is the case for a skyrmionium, target skyrmion, skyrmion bag, etc. Formally, we define the core of a skyrmion as the set of magnetic moments lying inside the contour. A skyrmion is then said to be comprised within another one if its core is a subset of the other's core.

This last step allows us to sort the skyrmions and build a tree-like graph. Such a graph is represented in Fig. 4.2 alongside the corresponding magnetic lattice and skyrmion contours. The graph can then be compared to a pre-generated database in order to automatically identify the detected structure of skyrmions.

4.2 Nucleation using an electric field

In this section we show how a femtosecond pulsed electric field can coherently nucleate a skyrmion. This mechanism was demonstrated by *Desplat et al.* [12].

At the start of the magnetization dynamics simulation the magnetic lattice is initialized in the ferromagnetic state with a single in-plane magnetic moment. This in-plane magnetic moment is required in order for the electric field to exert a torque on the magnetic moments of the lattice. Indeed as the electric field induces a DM-like interaction, non-collinear moments are needed for its effect to be non-zero. This in-plane moment is clearly artificial. A similar effect could be obtained by performing simulations at finite temperature. This would have the advantage of being physically more accurate. However it would also complexify the study

and the analysis of our results.

Throughout this section the applied external electric field is directed along the z-direction and is spatially homogeneous. The electric field is applied for a short period of time and is constant during that time. Mathematically we have

$$\vec{E}(x,y,z,t) = \begin{cases} E\hat{z} & \text{if } t \in [0, t_{\text{exc}}], \\ 0 & \text{otherwise.} \end{cases} \tag{4.3}$$

The magnetoelectric coupling constant is taken to be $\alpha = 10^{15}$ eVm/V as it is usually of that order.

Taking $J = 11$ meV, $K = 0.5J$ and $D = 0.44J$, the application of a 100-fs pulse with an electric field intensity of 16.5×10^{12} V/m leads to the nucleation of a skyrmion within 54 fs. The evolution of the topological charge and the total energy per magnetic moment is plotted in Fig. 4.3. Fig. 4.4 shows snapshots of the magnetic lattice at different key steps: initial configuration, nucleation, switching off of the electric field and relaxed final configuration. We see that at the time of nucleation the skyrmion is of minimal radius. We also see that, shortly after, the energy starts decreasing linearly with time. This is due to the fact that, after the nucleation, the skyrmion radius increases with time, increasing the domain boundary size. As the DMI is enhanced by the electric field, the non collinear domain boundary is energitically favored over the collinear ferromagnetic background. Switching off the electric field causes a discontinuity in the energy as the DMI is suddenly reduced.

After the off-swithing of the electric, the skyrmion remains stable.

If the intensity of the electric field is too low no skyrmion is nucleated. There therefore exists a minimal or threshold value for nucleation. We can use a bisection algorithm to determine this minimal value. For the values of K and D given above the minimal electric field intensity is 16.35×10^{12} V/m. This is an unrealistically large value as modern-day THz lasers can only go up to about 10^{10} V/m [32].

We can repeat the same procedure to find the minimal electric field intensity for various values of K and D. This gives us the phase diagram shown in Fig. 4.5 as a function of the reduced anisotropy and DMI constants $k = K/J$ and $d = D/J$. The colormap represents the minimal electric field intensity. When the DMI is too weak in comparison with the anisotropy skyrmions are not metastable and will relax into the ferromagnetic state after nucleation. This corresponds to region I in the phase diagram. The time between nucleation and annihilation depends on the electric field intensity and increases with it. A larger electric field will transfer more energy to the magnetic lattice and more time will be needed for it to dissipate this excess of energy and return into the ferromagnetic state (we recall that a skyrmion is an excitation of the ferromagnetic state).

When the DMI is too strong in comparison to the anisotropy the ground state

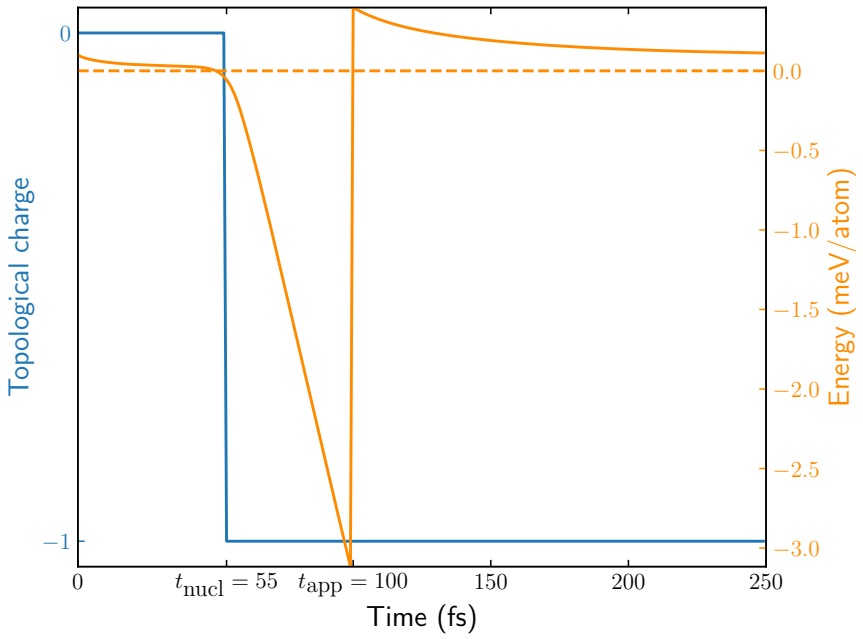

Figure 4.3: Time evolution of the topological charge and of the total energy per magnetic moment during the nucleation of a skyrmion by an electric field pulse. The reference zero energy is that of the ferromagnetic state.

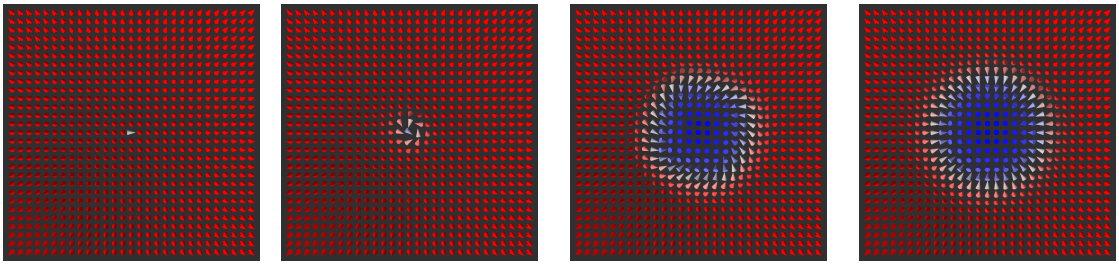

(a) Initial configuration (b) $t = 54$ fs (c) $t = 100$ fs (d) Final (relaxed) configuration

Figure 4.4: Snapshots of the magnetic lattice at different times during the nucleation of a skyrmion by an external electric field using a magnetic defect.

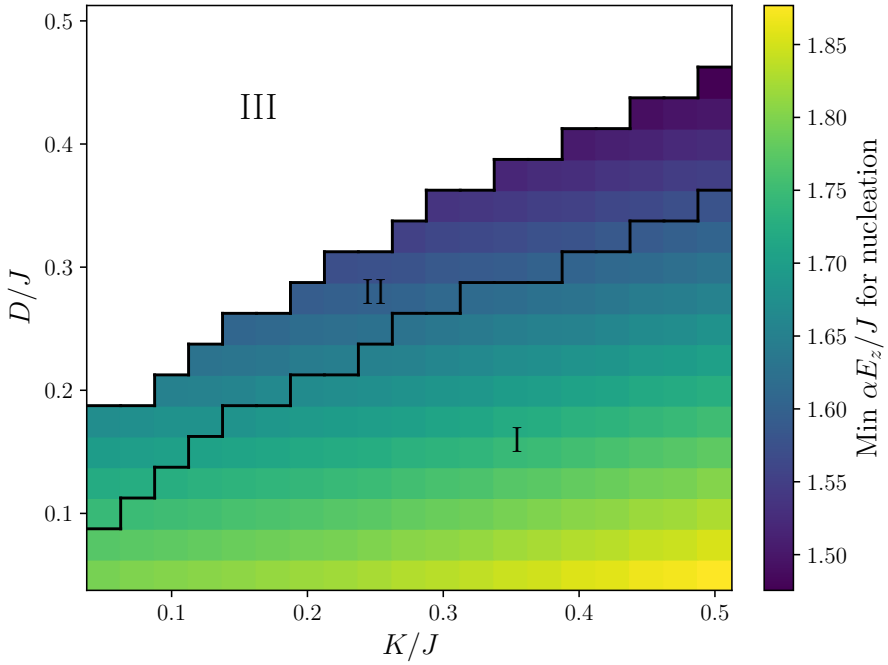

Figure 4.5: Phase diagram for nucleation of a skyrmion using a pulsed electric field of 100 fs. Regions I, II, III represents non-metastable skyrmions, metastable skyrmions and spin spiral phase respectively. This graph reproduces the one found in the supplementary material of Ref. [12].

switches from ferromagnetic to a Néel spin spiral and skyrmions can no longer exist. This transition from ferromagnetic to spin-spiral occurs at $d = 2\sqrt{k}/\pi$ [23]. Region III in the phase diagram corresponds to this spin-spiral state.

Finally region II corresponds to metastable skyrmions in a ferromagnetic background. The values for d and k taken for the example above lie in this region. By looking at regions I and II, we see that the minimal electric field for nucleation increases with the anisotropy but decreases with the DMI.

From the graph, we would ideally want a material with large values of K and D in order to have the smallest required electric field for nucleation. However for most systems both K and D are rather located at the bottom left of the graph. For example for Pd/Fe/Ir(111), *ab initio* simulations give $k \sim 0.12J$, $d \sim 0.18J$ [60].

4.3 Nucleation using Laguerre-Gauss beams

In the previous section, we were able to nucleate a skyrmion by applying a spatially-homogeneous electric field for a duration of 100 fs. However the minimal electric field is on the order of 10^{13} V/m which is quite large and we should seek to reduce this value. In this section we consider Laguerre-Gauss beams (as introduced in chapter 3), including the effect of the magnetic field. Our main motivation for the use of LG beams lies in that they carry orbital angular momentum and could transfer their angular momentum to the magnetic system. Furthermore LG-beams are spatially non-homogeneous This is in contrast to the spatially homogeneous electric field considered in the previous section. These two characteristics could reduce the minimal intensity for the nucleation of a skyrmion and even nucleate more diverse topological magnetic textures such as target skyrmions, skyrmion bags and higher-order skyrmions.

This section will be divided in two sub-sections. The first one is concerned with the simplified case of a Gaussian beam, which corresponds to a LG-beam with both azimuthal and radial numbers equal to zero ($l = 0, p = 0$). LG-beams with non-zero azimuthal numbers (and therefore non-zero orbital angular momentum) are considered in the second sub-section.

4.3.1 Case of a Gaussian beam

A Gaussian beam is a special case of LG-beam with $l = 0, p = 0$. The general expressions of the electric and magnetic fields given by Eq. (3.13), (3.21), (3.22)

become for $z = 0$

$$E(r, \phi, t) = \sqrt{\frac{2}{\pi}} \frac{2}{w_0} e^{-\frac{r^2}{w_0^2}} \cos(\omega t) \tag{4.4}$$

$$B_r(r, \phi, t) = 0 \tag{4.5}$$

$$B_\phi(r, \phi, t) = \sqrt{\frac{2}{\pi}} \frac{4r}{\omega w_0^3} e^{-\frac{r^2}{w_0^2}} \sin(\omega t). \tag{4.6}$$

For a first example we take $K = 0.5J$ and $D = 0.44J$ as in section 4.2. Skyrmions are metastable for this set of parameters. For the beam parameters, we take a width w_0 of 10 nm as it is comparable to the size of a skyrmion. The period is taken to be 400 fs. The beam is applied for a duration of 200 fs i.e. for half a period. The time dependence of the electric and magnetic fields are summarized in Fig. 4.6.

The time dependence is simple and permits a better eased understanding of the nucleation mechanism. It also prevents from a null time averaging of the effects of the excitation.The second half of a period, where the electric field is negative, would cancel the first half of the period, where the electric is positive. However, it can be experimentally challenging to generate such sub-cycle pulses.

Before proceeding to the simulation, a comment is to be made on the value of the parameters. For the chosen beam period, the wavelength is equal to $c \cdot T = 120$ μm, which is about 10^4 times larger than the beam waist w_0. Therefore these are classically not realistic parameters. However recent developments in the field a plasmonics opened the way towards subwavelength focusing of beams [22, 3]. A factor 40 between the spatial resolution of the beam and its wavelength has been achieved numerically [50]. Further development could lead to even larger factors. Nevertheless a factor 10^4, as in our case, do not seem feasible (or at least not in a near future). We chose to remain with this value of the beam waist as it could provide a basis to future works with either systems with larger skyrmion radii and/or beams with a smaller period which would render our beam wais values feasible.

When fixing the peak intensity of the electric field of the beam to 4.8×10^6 V/m a skyrmion is successfully nucleated, which is much lower than for a homogeneous beam, and experimentally accessible. Fig. 4.7 shows snapshots of the magnetic moments throughout the nucleation process. For this intensity of the electric field the peak intensity of the magnetic field is 52 T. This is a large value but it remains within reach, as the production of such high intensity fields has been experimentally demonstrated [32]. It must also be noted that the ratio of the electric and magnetic fields has been artificially boosted by the sub-wavelength beam waist size. Indeed, by examining Eqs. (4.4) and (4.6), we see that the ratio

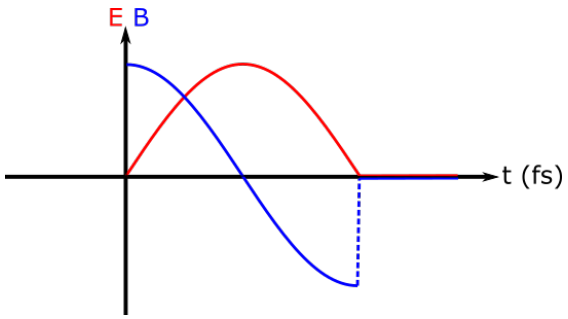

Figure 4.6: Time dependence of the electric and magnetic fields. The beam has a period of 400 fs.

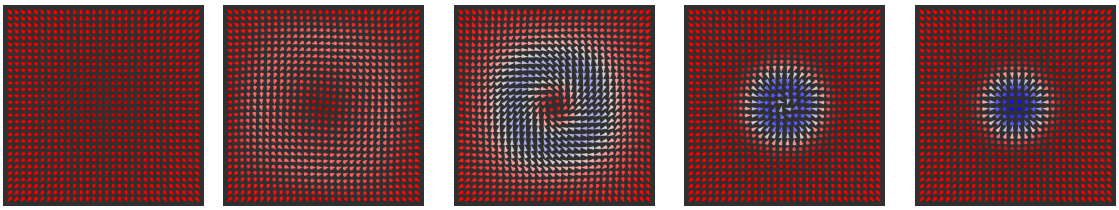

(a) $t = 0$ fs (b) $t = 100$ fs (c) $t = 200$ fs (d) $t = 400$ fs (e) $t = 5$ ps

Figure 4.7: Snapshots of the magnetic lattice during the nucleation of a skyrmion using a Gaussian beam.

B_ϕ/E scales as

$$B_\phi/E \propto 1/\omega w_0. \tag{4.7}$$

In future works, if a larger beam waist and/or a larger beam frequency is chosen, the intensity of the electric field might increase for a fixed magnetic field intensity.

A first remark has to be made here. In section 4.2 we introduced a magnetic defect in the initial configuration, to enable the electric field induced DMI to act. However, the magnetic field is able to exert a torque on the magnetic moments without any defect. Therefore the in-plane spin is no longer required and the simulation was carried out with all spins initially along the z-direction.

A second remark can be made considering the respective amplitude of the electric and magnetic fields and their impact on the magnetic lattice dynamics. In the extended Heisenberg Hamiltonian, the electric field contributes to an order of $\alpha\left\|\vec{E}\right\| \sim 4.8 \times 10^{-6}$ meV whereas the magnetic field contributes to an order of $\mu_s\left\|\vec{B}\right\| \sim 9.0$ meV. We see that the impact of the electric field on the magnetic moments can be neglected with respect to that of the magnetic field. We can further compare these orders of magnitude to the effective Heisenberg constant $J = 11meV$. We see that the Zeeman energy term (through which the magnetic field acts) is on par with the effective exchange. This further points out that the

magnetic field is the essential part of the nucleation process here. The mechanism of nucleation is sensibly different as well. The nucleation via an electric field, which was first detailed by Desplat and coworker [12], occurs through the modification of the effective DMI. This is *as if* we move through the phase diagram and momentarily switch to the spin spiral ground state which destabilizes the ferromagnetic state and gives the opportunity to nucleate a skyrmion. Here, with the magnetic field, the nucleation happens rather through a local reversal of the magnetization. This mechanism resembles much more a precessional magnetization reversal.

We mentioned earlier that the chosen beam waist is 10^4 smaller than its wavelength and the ratio B_ϕ/E scales as $1/\omega w_0$ (cfr. Eq. (4.7)). If by increasing the beam waist and/or its frequency the beam waist becomes comparable to its wavelength, the electric field intensity would be multiplied by 10^4, for a fixed magnetic field intensity. Despite this large increase, its effect on the magnetization dynamics would still be negligible as $\alpha\left\|\vec{E}\right\|$ would merely attain 0.1 meV. Therefore the magnetic field would remain the essential part of the beam regarding the nucleation process.

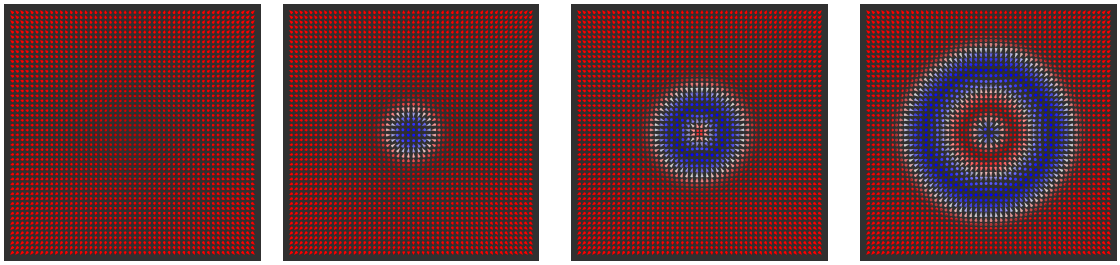

(a) $B_{\text{peak}} = 45$ T (b) $B_{\text{peak}} = 52$ T (c) $B_{\text{peak}} = 61$ T (d) $B_{\text{peak}} = 105$ T

Figure 4.8: Obtained final magnetic configurations after the application of a Gaussian beam for different peak intensities of the magnetic field.

As a first example we fixed the peak intensity of the magnetic field at 52 T and this resulted in a skyrmion. By increasing or decreasing it we can obtain different end results. The first few possible end magnetic configurations are shown in Fig. 4.8. Obviously when the peak intensity is below some threshold nothing is nucleated. Above that threshold a skyrmion is nucleated. When the peak intensity increases above a second threshold a skyrmionium is nucleated instead of a skyrmion. If we keep increasing the peak intensity we will get a different successive magnetic textures for larger threshold values. With this we are able to draw a graph representing the obtained magnetic texture as a function of the peak intensity of the applied beam. This is shown in Fig. 4.9. The labeling of the y-axis is arbitrary and is chosen to be monotonous with the beam intensity for clarity. To draw this figure, we performed spin dynamics simulations for each beam intensity,

and used the automatic identification algorithm developed in section 4.1 on the obtained magnetic texture.

We see that the relation between the beam intensity and the obtained magnetic texture is a piece-wise constant function.

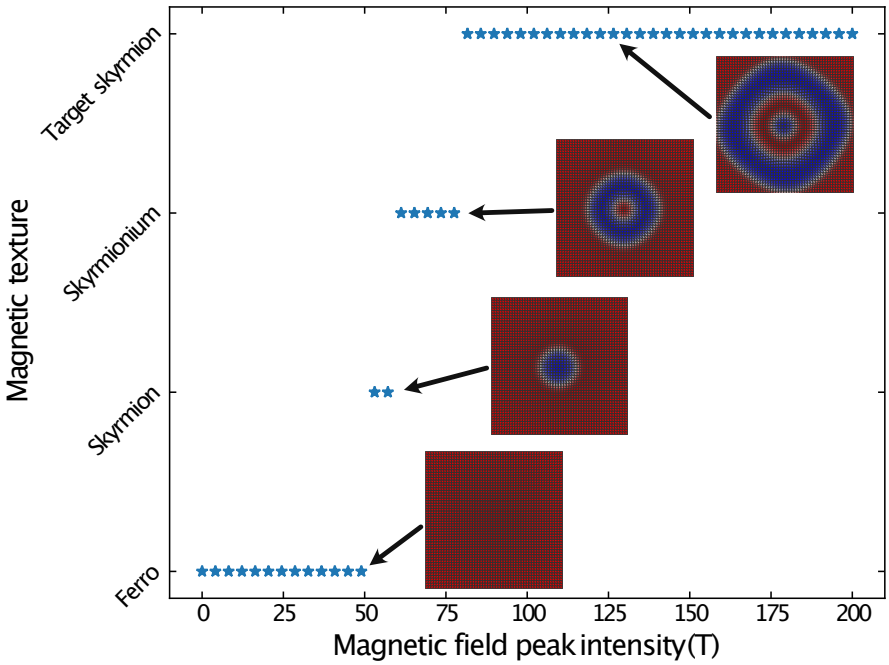

Figure 4.9: Nucleated magnetic texture as a function of the peak intensity of the magnetic field of the Gaussian beam.

Modified bisection algorithm

We will now present a modified bisection algorithm in order to determine the threshold values of the intensity of the beam for the nucleation of the different magnetic textures. It takes advantage efficiently of the piecewise constant behavior previously highlighted.

Let f be the function that for any value of the beam intensity associates to it the name of the nucleated magnetic texture (skyrmion, skymionium,...). Let a, b with $a < b$ be a lower and an upper bound defining a search-interval $[a, b]$ for the beam intensity. If $f(a) \neq f(b)$, there must exist (at least) one threshold value in the interval at which we have a change in the nucleated magnetic texture. As in a standard bisection method we look at the middle of the interval $c = (a + b)/2$. If $f(c)$ is equal to $f(a)$ then the search-interval can be reduced to $[c, b]$. If $f(c)$ is equal to $f(b)$ then the search-interval is rather reduced to $[a, c]$. In the last case

where $f(c)$ is neither equal to $f(a)$ nor to $f(b)$, the search-interval is divided in two subsequent search intervals $[a, c]$ and $[c, b]$. Each subsequent interval must contain (at least) one threshold as we have $f(a) \neq f(c)$ and $f(c) \neq f(b)$. This procedure is repeated until the search-intervals are reduced to satisfying accuracy.

This modified bisection can be written in pseudo-code as shown in Algorithm 1.

Algorithm 1 Modified bisection

Require: $a < b$

```
1:  procedure BISECTION(a, b)
2:      f_a ← f(a)
3:      f_b ← f(b)
4:      if f_a = f_b then
5:          return
6:      end if
7:      err ← b − a
8:      while err > tol do          ▷ tol is the tolerance on the threshold values
9:          c ← (a + b)/2
10:         f_c ← f(c)
11:         if f_a = f_c then
12:             a ← c
13:             f_a ← f_c
14:         else if f_b = f_c then
15:             b ← c
16:             f_b ← f_c
17:         else                                          ▷ f_c ≠ f_a, f_b
18:             BISECTION(a, c)
19:             BISECTION(c, b)
20:             return
21:         end if
22:         err ← b − a
23:     end while
24:     OUTPUT(a, b, f_a, f_b)
25: end procedure
```

Results

We are now able to identify the different magnetic textures possible to nucleate with a Gaussian beam and the corresponding beam intensity threshold for their

nucleation. This process can be carried out for several values of k and d and we can draw color plots similar to Fig. 4.5 from section 4.2.

We recall that we previously identified 3 regions in the $k - d$ plane (see Fig. 4.5). In the first region the ground state is ferromagnetic and skyrmions are not metastable but can be nucleated dynamically. In the second region, skyrmions become metastable. In the third and last region the ground state switches to a spin spiral and skyrmions no longer exist. As we use the automatic identification of topological magnetic textures algorithm which can only treat relaxed magnetic lattices, we have to restrict ourselves to region II.

The upper bound delimiting region II from region III is analytical and is given by $d_{\max}(k) = 2\sqrt{k}/\pi$. The lower bound $d_{\min}(k)$ delimiting region II from region I has no analytical expression (as far as I am aware of). Therefore it had to be determined numerically. This was performed by relaxing a skyrmion via spin-dynamics.

With these considerations in mind, we can plot colormaps of the threshold intensities in function of k and d. The threshold intensity for the nucleation of a single skyrmion is shown in Fig. 4.10. The solid red lines represent the limits of region II. Fig. 4.11 and 4.12 show the threshold peak intensity for the nucleation of skyrmionium and a target skyrmion. Blank squares indicate either that the threshold intensity lies above the maximum peak intensity investigated (which is 200 T) or that the magnetic texture cannot be nucleated. The latter occurs only for the nucleation of a skyrmionium with values of k comprised between 0.15 and 0.25. The skyrmionium cannot be nucleated as it gets broken down in 4 individual skyrmions. This is shown in Fig. 4.13. This is most certainly due to the use of a square lattice and would be different on an hexagonal lattice.

When examining Fig. 4.10, we see an abrupt change in the nucleation threshold intensity around $d \simeq 0.25$, which does not decrease further as d increases. This change is somewhat repeated in Figs. 4.11 and 4.12 but to a lesser extent. Two possible explanations for this odd behavior are either that this is a spurious numerical result, or there is actually a change in the behavior of the system. At the time of writing we were not able to resolve this.

Let us focus on the region above the abrupt change, which is roughly delimited by $0.25 < k < 0.5$. We see that the nucleation thresholds for a skyrmion or a skyrmionium do not vary much with d, whereas the threshold for a target skyrmion decreases strongly with increasing d. In order to explain this dependence, let us base ourselves on the profiles of the nucleated skyrmion, skyrmionium and target skyrmion displayed in Fig. 4.8. There are noticeably more non-collinear magnetic moments in the profile of the target skyrmion than in the profile of the other two. The DM interaction favors non-collinear configurations. Therefore a target skyrmion becomes more and more favorable energitically. It follows from this

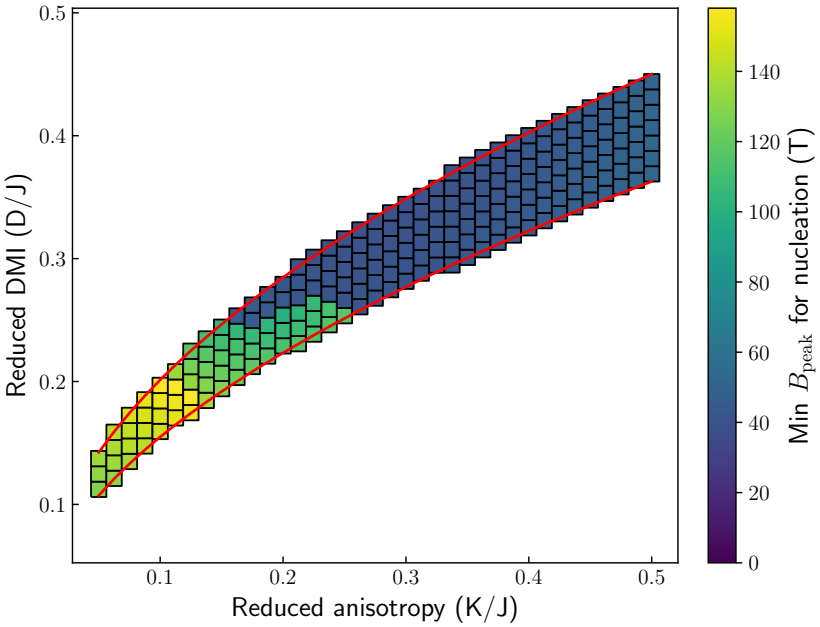

Figure 4.10: Threshold peak intensity of the magnetic field of the Gaussian beam for the nucleation of a skyrmion. The two red lines represent the limits of the skyrmion metastability region.

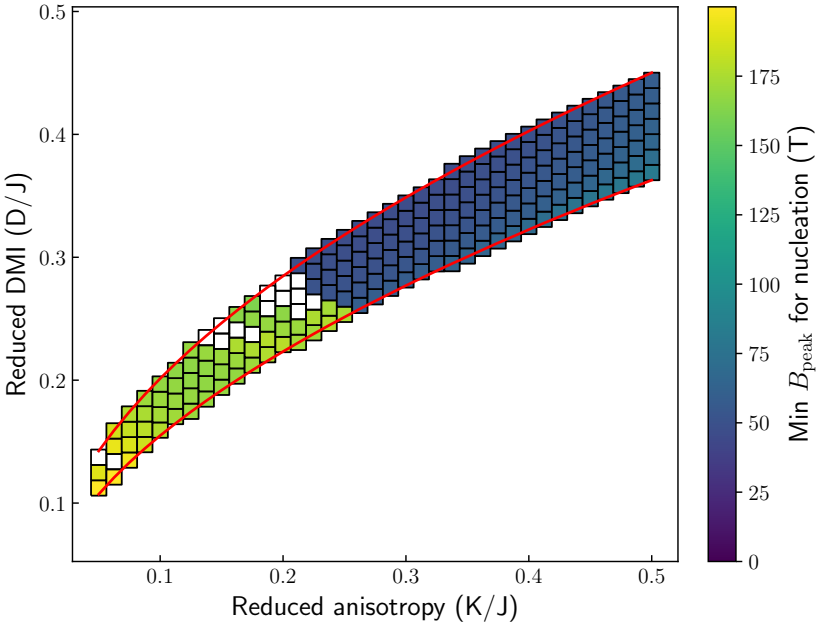

Figure 4.11: Threshold peak intensities of the magnetic field of the Gaussian beam for the nucleation of a skyrmionium.

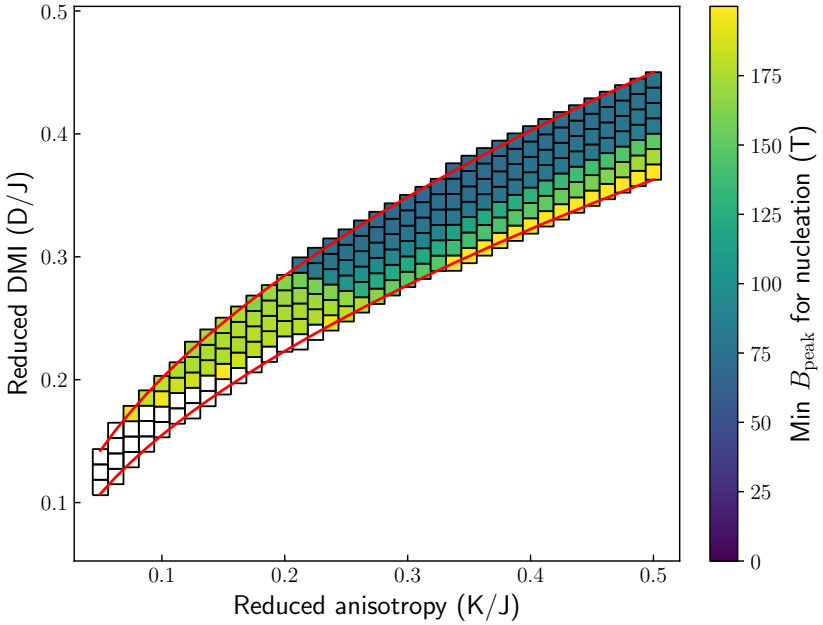

Figure 4.12: Threshold peak intensities of the magnetic field of the Gaussian beam for the nucleation of a target skyrmion.

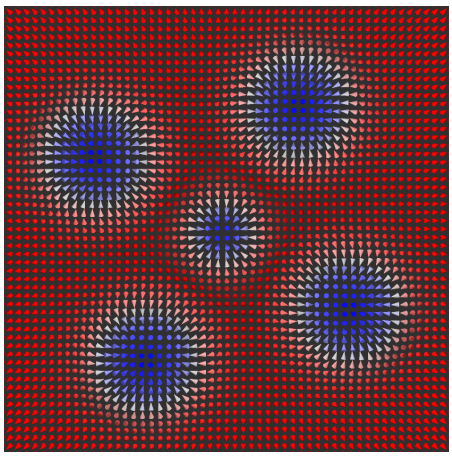

Figure 4.13: 5 skyrmions resulting from a target skyrmion whose skyrmionium was broken down in four individual skyrmions during the nucleation (for $k = 0.2$ and $d = 0.279$)

that the nucleation threshold intensity should also be impacted and decrease with increasing d, as it is indeed the case from Fig. 4.12.

4.3.2 Case of a Laguerre-Gauss beam with $l = 1$

We now carry on with the case a LG beam with $l = 1$ and $p = 0$. Contrary to the previous case of $l = 0$, here the beam is chiral as it rotates counterclockwise (cfr. Chapter 3). The general expressions of the electric and magnetic fields given by Eq. (3.13), (3.21), (3.22) becomes for $z = 0$

$$E(r, \phi, t) = \frac{4\sqrt{2}}{w_0^2\sqrt{\pi}} r e^{-\frac{r^2}{w_0^2}} \cos(\phi - \omega t) \tag{4.8}$$

$$B_r(r, \phi, t) = \frac{4\sqrt{2}}{\omega w_0^2\sqrt{\pi}} e^{-\frac{r^2}{w_0^2}} \cos(\phi - \omega t) \tag{4.9}$$

$$B_\phi(r, \phi, t) = \frac{4\sqrt{2}}{\omega w_0^2\sqrt{\pi}} \left(2\frac{r^2}{w_0^2} - 1\right) e^{-\frac{r^2}{w_0^2}} \sin(\phi - \omega t). \tag{4.10}$$

In the following, we take the same beam parameters as in the last section. For a first insight on the magnetic textures that can be nucleated through this change from $l = 0$ to $l = 1$, we choose $J = 11$ meV, $k = 0.5$ and $d = 0.44$. Fig. 4.14 shows the nucleated textures in function of the beam intensity. Several results are to be noted here. The first one is the asymmetry and the fact that we obtain completely dissimilar results as compared to the case of $l = 0$ (cfr. Fig. 4.9). The first texture to be nucleated is a single skyrmion which is offset with respect to the beam center. This single skyrmion can be nucleated at a smaller beam intensity than compared to the $l = 0$ beam case (~ 36 T for the former and ~ 52 for the latter).

When increasing the beam intensity, 2 skyrmions are nucleated. For $l = 0$ a skyrmionium is nucleated instead.

Repeating the same procedure as in Section 4.3.1, we can draw colorplots of the threshold beam intensities for the obtained textures (single skyrmion and 2 skyrmions) as a function of k and d. These plots are presented in Figs. 4.15 and 4.16. The blank squares in Fig. 4.16 indicate that the threshold for nucleation lies above the investigated maximum value (200 T). The first comment to be made is that the abrupt change noted in the skyrmion nucleation threshold for the $l = 0$ case (see Fig. 4.10 is absent here.

A second comment that can be made is with respect to the dependence of the nucleation thresholds with k and d. For Fig. 4.15, there is a strong dependence of the nucleation threshold on k and d for small values of k and d ($k \lesssim 0.2$, $d \lesssim 0.25$). For larger values, the nucleation threshold is almost constant. For Fig. 4.16, we see that the dependence of the nucleation threshold intensity is non-monotonous.

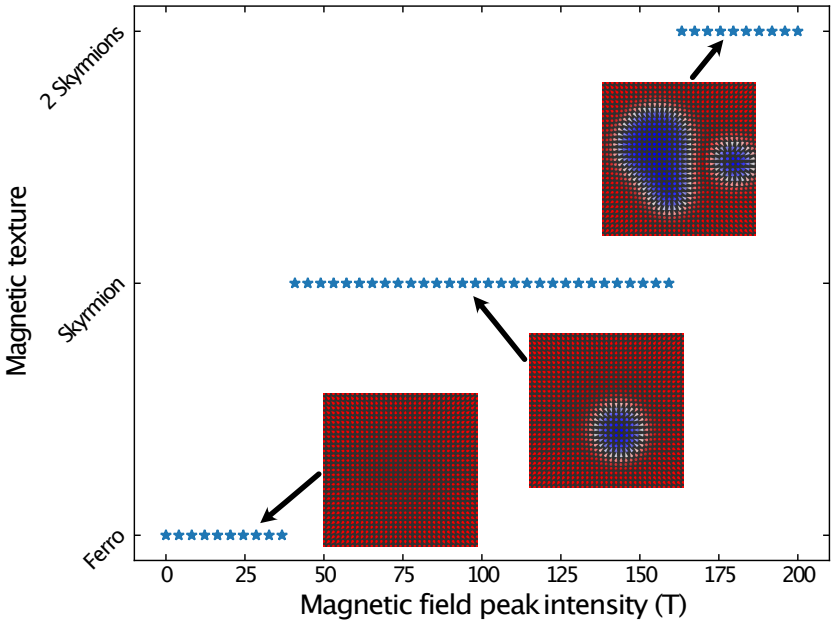

Figure 4.14: Nucleated magnetic texture as a function of the peak intensity of the magnetic field of the beam (l=1 case).

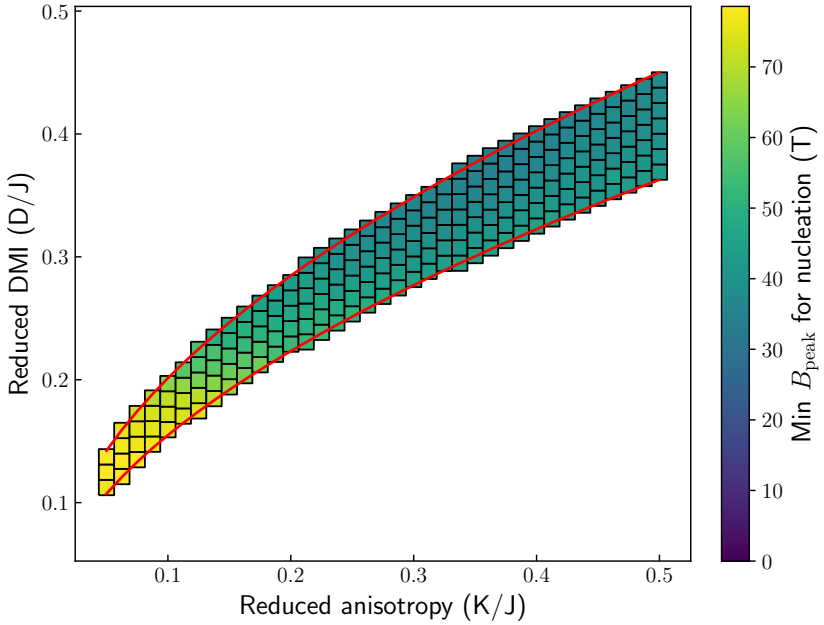

Figure 4.15: Threshold peak intensity of the magnetic field of the beam (l=1 case) for the nucleation of a skyrmion. The two red lines represent the limits of the skyrmion metastability region.

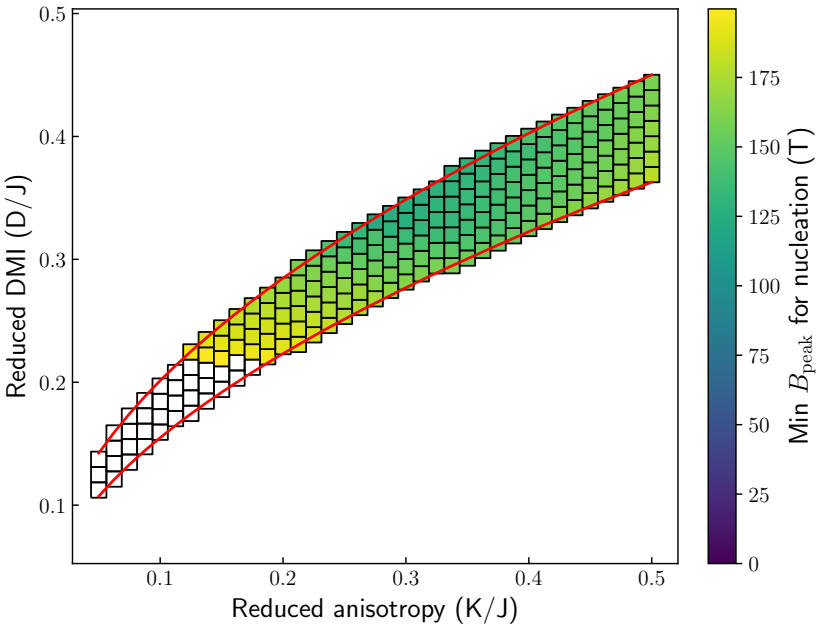

Figure 4.16: Threshold peak intensity of the magnetic field of the beam (l=1 case) for the nucleation of a 2 skyrmions complex.

This can be put in opposition with the results obtained for the case of the $l = 0$ beam.

As already mentioned, the nucleation threshold for a single skyrmion is decreased in comparison to the case $l = 0$. Let us recall the shape of the magnetic field derived in chapter 3 (see Fig. 3.3). For $l = 1$, the magnetic field forms two closed loops, each with opposite circulation. We can say that they possess opposite chiralities. Furthermore these loops rotate counter-clockwise around the beam center. When we investigated the nucleated textures as a function of the beam intensity, we saw that a single skyrmion is first obtained and then, for larger beam intensities, a second skyrmion is nucleated as well. This can be put in direct correlation with the two loops of the magnetic field and their chirality, one chirality favoring the skyrmion nucleation whereas the other is defavoring it.

We can conclude from this remark that the chirality of the LG beam effectively helps reducing the nucleation threshold.

5 Conclusion

In this Master's thesis, I study the nucleation of a skyrmion by an electric field pulse, either for a homogeneous beam, or for a shaped Laguerre-Gauss beam including the B field component. For the electric field nucleation we reproduced recent results obtained by *Desplat* and coworkers [12] and we managed to nucleate an isolated skyrmion with a 100-fs pulse. We also studied the dependence of the minimal electric field for nucleation as a function of the anisotropy and the DM interaction.

The nucleation with Laguerre-Gauss beams was studied in more detail. First, I derived the expression of the magnetic field starting from the expression of the electric field, using Maxwell's equations. The expressions of both the electric and magnetic fields were implemented in the Matjes code. Then I developed and implemented an algorithm for the automatic identification of topological magnetic textures, in order to analyze simulation results. This algorithm is generic and is able to detect and identify complex and composite topological magnetic textures with arbitrary topological charge.

Using a THz Laguerre-Gauss beam I showed it is possible to nucleate skyrmions and other magnetic textures (skyrmionium, target skyrmion and 2 or 5 skyrmions) and that this nucleation occurs through the magnetic field of the beam. We considered the case of a standard (isotropic) Gaussian beam and the case of a beam with a non-zero azimuthal number, carrying orbital angular momentum. Contrary to the nucleation with a spatially homogeneous electric field, I used LG beams with a spot size on the order of 10 mn which are therefore strongly non-homogeneous on the length scale of the simulation supercell. I developed and implemented a modified bisection algorithm in order to determine the minimal beam intensity needed to nucleate each of these magnetic textures. I also showed that the minimal beam intensity for the nucleation of a skyrmion is significantly lowered when including the magnetic field component and using a Laguerre Gauss beam. The orbital

angular momentum of the beam further reduces the minimal beam intensity for nucleation. This latter effect is due to the rotation of the beam.

To facilitate the experimental realization of skyrmion nucleation, one should also seek to reduce the intensity of the beam. In this work the minimal beam intensity for the nucleation resulted in a maximum magnetic field of ~ 30 T and a maximum electric field of $\sim 10^6$ V/m. The latter is easily accessible experimentally [32].

These encouraging results open the door to further work to approach experimental conditions. Indeed the chosen beam spot is not realistic as it is much smaller than the beam wavelength, and this also boosts the maximum B field "artificially". In order to tackle this, systems with larger skyrmion radii could be investigated, in larger simulation cells. Higher frequency beams could be employed to reduce the wavelength, spot size and simulation box, but this could also result in higher minimal beam intensities. The use of LG beams with larger values of l could counteract the frequency increase as the beam rotate at an angular speed $d\phi/dt = \omega/l$, which would allow the magnetization to follow the magnetic field more easily. Also as the beam spot size/wavelength ratio becomes more realistic, the ratio E/B would increase as well, leading to larger values of E for a fixed value of B.

Also I employed a simple effective magnetic model, with first nearest neighbor interactions only, in order to reduce the parameter space. More complex models could be explored with interactions beyond first nearest neighbor (Heisenberg exchange and DM interaction), and with frustrated exchange especially. This could permit the nucleation of antiskyrmions and higher order skyrmions, as these are not metastable in the effective model but can be stabilized with beyond first nearest neighbor interactions [13, 49, 60].

Laguerre-Gauss beams with azimuthal numbers equal only to either zero or one were considered. Larger values of l could lead to the nucleation of more complex textures, especially when considering magnetic models with beyond first nearest neighbor interactions. The nucleation of higher order skyrmions could realistically be envisioned.

Finally, a last comment can be made regarding the fact that LG beams with a longitudinal electric field were chosen. This choice was motivated by the results obtained for an homogeneous out-of-plane electric field pulse. However as we later shown, the electric field plays almost no role in the nucleation process and the magnetic field plays the main part. Beams with an in-plane electric field could be chosen instead in order to get experimentally more feasible beams to work with. However the magnetic field would no longer be purely in-plane and this could heavily impact the nucleation process.

Bibliography

[1] D Afanasiev, J R Hortensius, B A Ivanov, A Sasani, E Bousquet, Y M Blanter, R V Mikhaylovskiy, A V Kimel, and A D Caviglia. Ultrafast control of magnetic interactions via light-driven phonons. *Nature materials*, February 2021.

[2] Jack Y Araz, Juan Carlos Criado, and Michael Spannowsky. Identifying (anti-) skyrmions while they form. *arXiv preprint arXiv:2205.11535*, 2022.

[3] Takashi Arikawa, Shohei Morimoto, and Koichiro Tanaka. Focusing light with orbital angular momentum by circular array antenna. *Opt. Express*, 25(12):13728–13735, Jun 2017.

[4] M N Baibich, J M Broto, Albert Fert, Frédéric Nguyen Van Dau, Frédéric Petroff, P Eitenne, G Creuzet, A Friederich, and J Chazelas. Giant magnetoresistance of (001)Fe/(001)Cr magnetic superlattices. *Physical review letters*, 61(21):2472–2475, 1988.

[5] Eric Beaurepaire, J-C Merle, A Daunois, and J-Y Bigot. Ultrafast spin dynamics in ferromagnetic nickel. *Physical review letters*, 76(22):4250–4253, may 1996.

[6] G Berruto, I Madan, Y Murooka, G M Vanacore, E Pomarico, J Rajeswari, R Lamb, P Huang, A J Kruchkov, Y Togawa, T LaGrange, D McGrouther, H M Rønnow, and F Carbone. Laser-Induced skyrmion writing and erasing in an ultrafast Cryo-Lorentz transmission electron microscope. *Physical review letters*, 120(11):117201, March 2018.

[7] Olivier Boulle, Jan Vogel, Hongxin Yang, Stefania Pizzini, Dayane de Souza Chaves, Andrea Locatelli, Tevfik Onur Menteş, Alessandro Sala, Liliana Daniela Buda-Prejbeanu, Olivier Klein, Mohamed Belmeguenai, Yves Roussigné, Andreï Stashkevich, Salim-Mourad Chérif, Lucia Aballe, Michael Foerster, Mairbek Chshiev, Stéphane Auffret, Ioan Mihai Miron, and Gilles Gaudin. Room-temperature chiral magnetic skyrmions in ultrathin magnetic nanostructures. *Nature nanotechnology*, 11(5):449–454, January 2016.

[8] Felix Büttner, Christoforos Moutafis, Michael Schneider, Benjamin Krüger, C M Günther, J Geilhufe, C v Korff Schmising, J Mohanty, B Pfau, S Schaffert, André Bisig, M Foerster, T Schulz, C A F Vaz, J H Franken, H J M Swagten, Mathias Kläui, and Stefan Eisebitt. Dynamics and inertia of skyrmionic spin structures. *Nature physics*, 11(3):225–228, mar 2015.

[9] Felix Büttner, Bastian Pfau, Marie Böttcher, Michael Schneider, Giuseppe Mercurio, Christian M Günther, Piet Hessing, Christopher Klose, Angela Wittmann, Kathinka Gerlinger, Lisa-Marie Kern, Christian Strüber, Clemens von Korff Schmising, Josefin Fuchs, Dieter Engel, Alexandra Churikova, Siying Huang, Daniel Suzuki, Ivan Lemesh, Mantao Huang, Lucas Caretta, David Weder, John H Gaida, Marcel Möller, Tyler R Harvey, Sergey Zayko, Kai Bagschik, Robert Carley, Laurent Mercadier, Justine Schlappa, Alexander Yaroslavtsev, Loïc Le Guyarder, Natalia Gerasimova, Andreas Scherz, Carsten Deiter, Rafael Gort, David Hickin, Jun Zhu, Monica Turcato, David Lomidze, Florian Erdinger, Andrea Castoldi, Stefano Maffessanti, Matteo Porro, Andrey Samartsev, Jairo Sinova, Claus Ropers, Johan H Mentink, Bertrand Dupé, Geoffrey S D Beach, and Stefan Eisebitt. Observation of fluctuation-mediated picosecond nucleation of a topological phase. *Nature materials*, 20(1):30–37, January 2021.

[10] Sang-Wook W Cheong and Maxim Mostovoy. Multiferroics: a magnetic twist for ferroelectricity. *Nature materials*, 6(1):13–20, 2007.

[11] A Crépieux and Claudine Lacroix. Dzyaloshinsky–Moriya interactions induced by symmetry breaking at a surface. *Journal of magnetism and magnetic materials*, 182(3):341–349, 1998.

[12] L Desplat, S Meyer, J Bouaziz, P M Buhl, S Lounis, B Dupé, and P-A Hervieux. Mechanism for ultrafast electric-field driven skyrmion nucleation. *Physical review. B, Condensed matter*, 104(6):L060409, aug 2021.

[13] B Dupé, C N Kruse, T Dornheim, and S Heinze. How to reveal metastable skyrmionic spin structures by spin-polarized scanning tunneling microscopy. *New Journal of Physics*, 18(5):055015, may 2016.

[14] I Dzialoshinskii. A thermodynamic theory of "weak" ferromagnetism of antiferromagnetics. *The Journal of physics and chemistry of solids*, 4(4):241–255, 1958.

[15] Olle Eriksson, Anders Bergman, Lars Bergqvist, and Johan Hellsvik. *Atomistic spin dynamics: foundations and applications*. Oxford university press, 2017.

[16] R F L Evans, W J Fan, P Chureemart, T A Ostler, M O A Ellis, and R W Chantrell. Atomistic spin model simulations of magnetic nanomaterials. *Journal of Physics: Condensed Matter*, 26(10):103202, feb 2014.

[17] Albert Fert, Vincent Cros, and João Sampaio. Skyrmions on the track. *Nature nanotechnology*, 8(3):152–156, 2013.

[18] M. Först, R. I. Tobey, S. Wall, H. Bromberger, V. Khanna, A. L. Cavalieri, Y.-D. Chuang, W. S. Lee, R. Moore, W. F. Schlotter, J. J. Turner, O. Krupin, M. Trigo, H. Zheng, J. F. Mitchell, S. S. Dhesi, J. P. Hill, and A. Cavalleri. Driving magnetic order in a manganite by ultrafast lattice excitation. *Phys. Rev. B*, 84:241104, Dec 2011.

[19] Enrique J Galvez. Gaussian beams. Master's thesis, Colgate University, apr 2006.

[20] Mohsin Ganaie and Mohammad Zulfequar. Study of morphological, electrical and optical behaviour of amorphous chalcogenide semiconductor. In Jagannathan Thirumalai and Sergey Ivanovich Pokutnyi, editors, *Advances in Condensed-Matter and Materials Physics*, chapter 4. IntechOpen, Rijeka, 2020.

[21] T L Gilbert. A phenomenological theory of damping in ferromagnetic materials. *IEEE transactions on magnetics*, 40(6):3443–3449, nov 2004.

[22] Reinier W. Heeres and Valery Zwiller. Subwavelength focusing of light with orbital angular momentum. *Nano Letters*, 14(8):4598–4601, 08 2014.

[23] Changhoon Heo, Nikolai S. Kiselev, Ashis Kumar Nandy, Stefan Blügel, and Theo Rasing. Switching of chiral magnetic skyrmions by picosecond magnetic field pulses via transient topological states. *Scientific Reports*, 6(1):27146, 2016.

[24] Pin-Jui Hsu, André Kubetzka, Aurore Finco, Niklas Romming, Kirsten von Bergmann, and Roland Wiesendanger. Electric-field-driven switching of individual magnetic skyrmions. *Nature nanotechnology*, 12(2):123–126, nov 2016.

[25] I A Iakovlev, O M Sotnikov, and V V Mazurenko. Supervised learning approach for recognizing magnetic skyrmion phases. *Physical review. B, Condensed matter*, 98(17):174411, nov 2018.

[26] Hiroshi Imamura, Patrick Bruno, and Yasuhiro Utsumi. Twisted exchange interaction between localized spins embedded in a one- or two-dimensional electron gas with rashba spin-orbit coupling. *Physical Review B: Condensed Matter and Materials Physics*, 69(12):121303, mar 2004.

[27] S L Johnson, M Savoini, P Beaud, G Ingold, U Staub, F Carbone, L Castiglioni, M Hengsberger, and J Osterwalder. Watching ultrafast responses of structure and magnetism in condensed matter with momentum-resolved probes. *Structural dynamics (Melville, N.Y.)*, 4(6):061506, November 2017.

[28] S. L. Johnson, M. Savoini, P. Beaud, G. Ingold, U. Staub, F. Carbone, L. Castiglioni, M. Hengsberger, and J. Osterwalder. Watching ultrafast responses of structure and magnetism in condensed matter with momentum-resolved probes. *Structural Dynamics*, 4(6):061506, 2017.

[29] N Kazantseva, D Hinzke, Ulrich Nowak, Roy W Chantrell, and O Chubykalo-Fesenko. Atomistic models of ultrafast reversal. *Physica Status Solidi*, 244(12):4389–4393, December 2007.

[30] Frederic Keffer. Moriya interaction and the problem of β MnS. *Phys. Rev.*, 126:896, 1962.

[31] Jacob B. Khurgin. Fundamental limits of hot carrier injection from metal in nanoplasmonics. *Nanophotonics*, 9(2):453–471, 2020.

[32] Anastasios D. Koulouklidis, Claudia Gollner, Valentina Shumakova, Vladimir Yu. Fedorov, Audrius Pugžlys, Andrius Baltuška, and Stelios Tzortzakis. Observation of extremely efficient terahertz generation from mid-infrared two-color laser filaments. *Nature Communications*, 11(1):292, 2020.

[33] Philipp Kurz. *Non-Collinear Magnetism at Surfaces and in Ultrathin Films*. PhD thesis, University Aachen, 2004.

[34] J Ping Liu, Zhidong Zhang, and Guoping Zhao. *Skyrmions: topological structures, properties, and applications*. CRC Press, 2016.

[35] Yahui Liu, Zhengmeng Xu, Lin Liu, Kai Zhang, Yang Meng, Yuanwei Sun, Peng Gao, Hong-Wu Zhao, Qian Niu, and J Li. Switching magnon chirality in artificial ferrimagnet. *Nature communications*, 13(1):1264, March 2022.

[36] Shijiang Luo, Min Song, Xin Li, Yue Zhang, Jeongmin Hong, Xiaofei Yang, Xuecheng Zou, Nuo Xu, and Long You. Reconfigurable skyrmion logic gates. *Nano letters*, 18(2):1180–1184, feb 2018.

[37] Marder. *Condensed Matter Physics*. Wiley, second edition, 2010.

[38] Tim Matthies, Alexander F Schäffer, Thore Posske, Roland Wiesendanger, and Elena Y Vedmedenko. Topological characterization of dynamic chiral magnetic textures using machine learning. *Physical Review Applied*, 17(5):054022, may 2022.

[39] Sebastian Meyer. *Complex spin structures in frustrated ultrathin films*. PhD thesis, Kiel University, 2020.

[40] Joel S. Miller. Organic- and molecule-based magnets. *Materials Today*, 17(5):224–235, 2014.

[41] Tôru Moriya. Anisotropic superexchange interaction and weak ferromagnetism. *Physics Review*, 120(1):91–98, oct 1960.

[42] Loic Mougel, Patrick M Buhl, Ryohei Nemoto, Timofey Balashov, Marie Hervé, Julian Skolaut, Toyo Kazu Yamada, Bertrand Dupé, and Wulf Wulfhekel. Instability of skyrmions in magnetic fields. *Applied physics letters*, 116(26):262406, jun 2020.

[43] S Mühlbauer, B Binz, F Jonietz, Christian Pfleiderer, Achim Rosch, A Neubauer, R Georgii, and P Böni. Skyrmion lattice in a chiral magnet. *Science*, 323(5916):915–919, 2009.

[44] Jan Müller. Magnetic skyrmions on a two-lane racetrack. *New journal of physics*, 19(2):025002, feb 2017.

[45] Markus Münzenberg. The missing link. *Nature Reviews Physics*, 1(38):105–106, 2019.

[46] Stuart Parkin, Masamitsu Hayashi, and Luc Thomas. Magnetic Domain-Wall racetrack memory. *Science*, 320(5873):190–194, 2008.

[47] Déborah Persuy. *Nanoscopie résolue en temps : étude de la réponse spatiale et temporelle pour l'imagerie ultra-rapide*. PhD thesis, Université de Strasbourg, 2015.

[48] Niklas Romming, Christian Hanneken, Matthias Menzel, Jessica E Bickel, Boris Wolter, Kirsten von Bergmann, André Kubetzka, and Roland Wiesendanger. Writing and deleting single magnetic skyrmions. *Science*, 341(6146):636–639, 2013.

[49] Levente Rózsa, Krisztián Palotás, András Deák, Eszter Simon, Rocio Yanes, László Udvardi, László Szunyogh, and Ulrich Nowak. Formation and stability of metastable skyrmionic spin structures with various topologies in an ultrathin film. *Phys. Rev. B*, 95:094423, Mar 2017.

[50] Kyosuke Sakai, Takeaki Yamamoto, and Keiji Sasaki. Nanofocusing of structured light for quadrupolar light-matter interactions. *Scientific reports*, 8(1):7746, may 2018.

[51] Jun John Sakurai. *Advanced quantum mechanics*. Pearson Education India, 2006.

[52] Jun John Sakurai and Napolitano Jim. *Modern quantum mechanics*. Pearson Education India, 2011.

[53] J S Salcedo-Gallo, C C Galindo-González, and E Restrepo-Parra. Deep learning approach for image classification of magnetic phases in chiral magnets. *Journal of magnetism and magnetic materials*, 501:166482, may 2020.

[54] João Sampaio, Vincent Cros, Stanislas Rohart, André Thiaville, and Albert Fert. Nucleation, stability and current-induced motion of isolated magnetic skyrmions in nanostructures. *Nature nanotechnology*, 8(11):839–844, 2013.

[55] Marine Schott, Anne Bernand-Mantel, Laurent Ranno, Stefania Pizzini, Jan Vogel, Hélène Béa, Claire Baraduc, Stéphane Auffret, Gilles Gaudin, and Dominique Givord. The skyrmion switch: Turning magnetic skyrmion bubbles on and off with an electric field. *Nano letters*, 17(5):3006–3012, may 2017.

[56] Qiming Shao, Peng Li, Luqiao Liu, Hyunsoo Yang, Shunsuke Fukami, Armin Razavi, Hao Wu, Kang Wang, Frank Freimuth, Yuriy Mokrousov, Mark D Stiles, Satoru Emori, Axel Hoffmann, Johan Åkerman, Kaushik Roy, Jian-Ping Wang, See-Hun Yang, Kevin Garello, and Wei Zhang. Roadmap of Spin–Orbit torques. *IEEE transactions on magnetics*, 57(7):1–39, jul 2021.

[57] Florian Siegrist, Julia A Gessner, Marcus Ossiander, Christian Denker, Yi-Ping Chang, Malte C Schröder, Alexander Guggenmos, Yang Cui, Jakob Walowski, Ulrike Martens, J K Dewhurst, Ulf Kleineberg, Markus Münzenberg, Sangeeta Sharma, and Martin Schultze. Light-wave dynamic control of magnetism. *Nature*, 571(7764):240–244, July 2019.

[58] Kyung Mee Song, Jae-Seung Jeong, Biao Pan, Xichao Zhang, Jing Xia, Sunkyung Cha, Tae-Eon Park, Kwangsu Kim, Simone Finizio, Jörg Raabe, et al. Skyrmion-based artificial synapses for neuromorphic computing. *Nature Electronics*, 3(3):148–155, 2020.

[59] S R Tauchert, M Volkov, D Ehberger, D Kazenwadel, M Evers, H Lange, A Donges, A Book, W Kreuzpaintner, U Nowak, and P Baum. Polarized phonons carry angular momentum in ultrafast demagnetization. *Nature*, 602(7895):73–77, feb 2022.

[60] S. von Malottki, B. Dupé, P. F. Bessarab, A. Delin, and S. Heinze. Enhanced skyrmion stability due to exchange frustration. *Scientific Reports*, 7(1):12299, 2017.

[61] Jakob Walowski and Markus Münzenberg. Perspective: Ultrafast magnetism and THz spintronics. *Journal of applied physics*, 120(14):140901, oct 2016.

[62] Guoqiang Yu, Pramey Upadhyaya, Xiang Li, Wenyuan Li, Se Kwon Kim, Yabin Fan, Kin L Wong, Yaroslav Tserkovnyak, Pedram Khalili Amiri, and Kang L Wang. Room-Temperature creation and Spin-Orbit torque manipulation of skyrmions in thin films with engineered asymmetry. *Nano letters*, feb 2016.

[63] Xichao Zhang, Motohiko Ezawa, and Yan Zhou. Magnetic skyrmion logic gates: conversion, duplication and merging of skyrmions. *Scientific reports*, 5:9400, jan 2015.